

MMME: A Spontaneous Multi-Modal Micro-Expression Dataset Enabling Visual-Physiological Fusion

Chuang Ma^a, Yu Pei^a, Jianhang Zhang^a, Shaokai Zhao^a, Bowen Ji^b, Liang Xie^a, Ye Yan^a and Erwei Yin^{a,*}

^aThe Defense Innovation Institute, Academy of Military Sciences, Beijing, China

^bNorthwestern Polytechnical University, Xi'an, China

ARTICLE INFO

Keywords:

Micro-Expression
Physiological Signals
Multi-Modality Fusion
Recognition and Spotting
Concordance

ABSTRACT

Micro-expressions (MEs) are subtle, fleeting nonverbal cues that reveal an individual's genuine emotional state. Their analysis has attracted considerable interest due to its promising applications in fields such as healthcare, criminal investigation, and human-computer interaction. However, existing ME research is limited to single visual modality, overlooking the rich emotional information conveyed by other physiological modalities, resulting in ME recognition and spotting performance far below practical application needs. Therefore, exploring the cross-modal association mechanism between ME visual features and physiological signals (PS), and developing a multimodal fusion framework, represents a pivotal step toward advancing ME analysis. This study introduces a novel ME dataset, MMME, which, for the first time, enables synchronized collection of facial action signals (MEs), central nervous system signals (EEG), and peripheral PS (PPG, RSP, SKT, EDA, and ECG). By overcoming the constraints of existing ME corpora, MMME comprises 634 MEs, 2,841 macro-expressions (MaEs), and 2,890 trials of synchronized multimodal PS, establishing a robust foundation for investigating ME neural mechanisms and conducting multimodal fusion-based analyses. Extensive experiments validate the dataset's reliability and provide benchmarks for ME analysis, demonstrating that integrating MEs with PS significantly enhances recognition and spotting performance. To the best of our knowledge, MMME is the most comprehensive ME dataset to date in terms of modality diversity. It provides critical data support for exploring the neural mechanisms of MEs and uncovering the visual-physiological synergistic effects, driving a paradigm shift in ME research from single-modality visual analysis to multimodal fusion. The dataset will be publicly available upon acceptance of this paper.

1. Introduction

Emotions play a pivotal role in regulating human behavior and cognition, significantly influencing decision-making, social interactions, and mental health [1]. As a complex and multimodal phenomenon, emotions are expressed through a variety of external and internal activities [2]. External expressions encompass facial expressions, verbal communication, and body language, while internal responses include physiological changes such as central nervous system signals (e.g., electroencephalography) and peripheral nervous system signals (e.g., electrocardiography, electrodermal activity, and respiration). Emotion recognition involves analyzing these data to identify and interpret an individual's emotional state, with potential applications spanning diverse fields such as human-computer interaction, virtual reality, healthcare, and education.

In contemporary society, cultural norms, social expectations, and professional demands often compel individuals to conceal or suppress their genuine emotions through controlled facial expressions, body language, or verbal responses, making it challenging to accurately identify an individual's emotional states [3]. According to Ekman's theory

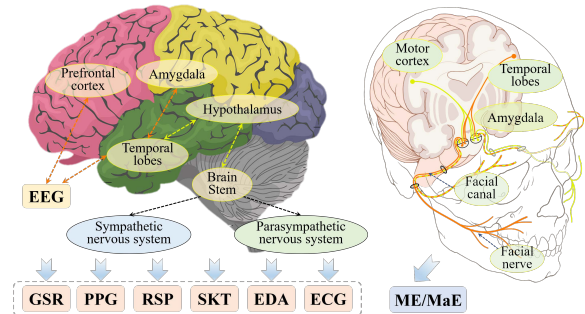


Figure 1: Signal generation and transmission pathway of emotional responses: from central nervous system activation (e.g., cerebral cortex and amygdala) to autonomic and peripheral nervous system responses, leading to physiological changes and facial micro-expressions.

of emotion [4], suppressed emotions may be unconsciously revealed through brief and subtle facial muscle movements, known as micro-expressions (MEs). MEs are fleeting facial changes, lasting only 1/25 to 1/2 a second (s), often too subtle to be detected by the naked eye [5]. These involuntary expressions typically surface when individuals attempt to conceal their true emotions, especially in high-pressure scenarios such as interrogations, negotiations, or intense social interactions. From a neurobiological perspective, MEs result from the interplay between voluntary facial expressions, controlled by the pyramidal system, and involuntary

*Corresponding author

✉ ustb_machuang@163.com (C. Ma); peiyu1995@buaa.edu.cn (Y. Pei);
15225746916@163.com (J. Zhang); lnkzsk@126.com (S. Zhao);
bwji@nwpu.edu.cn (B. Ji); xie1nudd@gmail.com (L. Xie); yy_taiic@163.com
(Y. Yan); yinerwei1985@gmail.com (E. Yin)
ORCID(s): 0000-0002-5741-2036 (C. Ma)

expressions, governed by the extrapyramidal system [6, 7], as illustrated in Fig. 1. This distinctive neurophysiological mechanism positions MEs as a vital indicator of psychological and physiological stress responses [8]. Concurrently, when individuals experience emotional fluctuations, their physiological signals (PS) also exhibit significant patterns of change [9]. For instance, electroencephalography (EEG) records brain activity through scalp electrodes, capturing dynamic changes in brain activity across different emotional states [10–12]. Electrocardiography (ECG) measures the heart’s electrical activity via skin electrodes, reflecting heart rate variability (HRV) and arrhythmias that are closely linked to emotional states [13]. Additionally, electrodermal activity (EDA), which indirectly measures sweat gland activity, serves as a key indicator of sympathetic nervous system activation and is widely used in deception detection [14]. Respiration (RSP) patterns correlate with emotions: irregular breathing often signals negative arousal (*e.g.*, tension or fear), while slower rates suggest relaxation [15]. Skin temperature (SKT) is a useful predictor of emotional states mediated by the autonomic nervous system and is frequently associated with heightened tension or excitement [16]. Li *et al.* [17] argued that the high ecological validity of multimodal data facilitated further research on the implementation of ME analysis in practical applications and physiologically-based ME mechanisms. Similarly, Zhang *et al.* [18] suggested that the integration of multimodal signals in ME analysis has the potential to overcome certain limitations inherent in existing visual corpora. From a multimodal fusion perspective, combining MEs with PS, including both central and peripheral nervous system signals, not only enables a more comprehensive understanding of the relationships between MEs and PS but also improves the accuracy of emotion recognition. Additionally, it increases the robustness of systems in real-world scenarios where data may be incomplete or ambiguous.

However, in the field of ME analysis, despite the increasing emphasis on multimodal fusion in recent years, research on MEs and PS continues to proceed largely in isolation, lacking a systematic framework for integrated analysis. This research gap can be attributed to two key factors. First, there is currently a lack of publicly available comprehensive ME datasets that incorporate synchronously acquired MEs and multiple PS. Second, the intrinsic relationship and concordance between MEs and PS have yet to be fully explored and validated. Therefore, developing a spontaneous multimodal ME dataset that synchronously records facial MEs and multiple PS would provide a crucial data foundation for investigating their underlying relationships and neurophysiological mechanisms, offering both theoretical insights and practical applications. Constructing a high-quality multimodal emotion dataset with scientific value requires careful consideration of key factors, including data synchronization, ecological validity, and sample size. First, ensuring synchronized data collection is essential. The variations in MEs and PS are often transient and rapid. MEs typically last between 40 milliseconds (ms) and 500

ms, while physiological signals, such as EEG and ECG, are recorded at high sampling rates, often reaching the kilohertz range. Therefore, synchronized acquisition ensures precise temporal alignment between different modalities, facilitating the analysis of their dynamic interrelationships. Second, the ecological validity of emotion induction experiments plays a crucial role in data quality. The natural elicitation of MEs is particularly challenging, as their occurrence is influenced by multiple factors, including the experimental environment, stimulus materials, and individual differences [19]. To enhance data authenticity and reliability, scientifically validated emotion induction paradigms—such as video-based stimuli, facial feedback mechanisms, or immersive interactive scenarios—should be employed. Finally, sample size directly impacts dataset generalizability and model robustness. Given the low occurrence rate of MEs, data collection processes are prone to class imbalance issues [20]. Thus, it is essential to construct a dataset that is not only sufficiently large but also well-balanced across categories to ensure the model’s stability and applicability.

Building upon the above considerations, we developed a multimodal dataset that synchronously captures human facial behavioral signals (MEs), central neural signals (EEG), and multiple peripheral physiological signals (PERI-PS)—including ECG, EDA, RSP, SKT, and PPG—to explore the advantages of multimodal fusion for emotion recognition. The dataset was validated and evaluated using several state-of-the-art algorithms. Additionally, we performed a comprehensive analysis of the correlations between MEs and PS under emotion-elicited conditions, aiming to elucidate the underlying interaction mechanisms across modalities.

The main contributions of this study are as follows:

1. Development of the MMME Dataset: We constructed a multimodal ME dataset, referred to as MMME, which integrates facial MEs, EEG, and multiple PERI-PS. This dataset not only overcame the limitations of relying solely on visual signals for ME analysis but also facilitated the development of more comprehensive and accurate emotion representation models. Furthermore, it enabled an exploration of the dynamic fusion mechanisms underlying emotional changes.
2. Exploring the concordance between MEs and PS: To effectively integrate visual and physiological features, we investigated whether MEs and PS exhibited synchronized variations during emotional responses. This analysis provided insights into their intrinsic relationships and underlying mechanisms, validating the applicability of the multichannel expression of emotion theory in the field of MEs.
3. Validation of dataset effectiveness: We conducted ME recognition and spotting tasks on the proposed dataset, employing both unimodal and multimodal fusion approaches. The experimental results demonstrate the efficacy of our multimodal fusion strategy in ME analysis, confirming the dataset’s high quality and establishing a reliable benchmark.

Table 1

The current spontaneous micro-expression databases. The information about our dataset is provided in the last row

Database	Year	Subjects		Characteristics of the Sample				Equipment	Annotation		Download URL
		Num	Eth	Num	Resolution	Sampling rate	Modality		Emotion	AU	
SMIC [21]	2013	16	Y	164	640 × 480	100 fps	HS-RGB	PixeLINK L-B774U camera	Pos(51) Neg(70) Sur(43)	-	https://www oulu.fi/en/university/faculties-and-units/faculty-information-technology-and-electrical-engineering/center-for-machine-vision-and-signal-analysis
		8		71	640 × 480	25 fps	RGB	Standard web camera	Pos(28) Neg(23) Sur(20)		
		8		71	640 × 480	25 fps	NIR	Near-infrared camera	Pos(28) Neg(24) Sur(20)		
CASME [22]	2013	19	N	195	1,280 × 720	60 fps	RGB	BenQ M31 camera	Amu(5) Dis(88) Fea(2)	12+	http://casme.psych.ac.cn/casme/c1
					640 × 480	60 fps	RGB	Point Grey GRAS-03K2C camera	Con(3) Sad(6) Ten(28) Sur(20) Rep(40)		
CASME II [23]	2014	26	N	247	640 × 480	200 fps	RGB	Point Grey GRAS-03K2C camera	Hap(33) Dis(60) Sur(25) Rep(27) Oth(102)	11+	http://casme.psych.ac.cn/casme/c2
SAMM [24]	2016	32	Y	159	2,040 × 1,080	200 fps	Grayscale	Basler Ace acA2000-340km camera	Hap(24) Dis(8) Fea(7) Ang(20) Sur(13) Sad(3) Oth(84)	ALL	https://helward.mmu.ac.uk/STAFF/M.Yap/dataset.php
MEVIEW [25]	2017	16	N	29	1,280 × 720	30 fps	RGB	-	Hap(4) Dis(1) Fea(3) Ang(1) Sur(8) Con(4) Unc(7)	7	https://cmp.felk.cvut.cz/cechj/ME/
CAS(ME) ² [26]	2018	22	N	57	640 × 480	30 fps	RGB	Logitech Pro C920 camera	Pos(8) Neg(21) Sur(9) Oth(19)	28	http://casme.psych.ac.cn/casme/c3
MMEW [27]	2021	36	N	300	1,920 × 1,080	90 fps	RGB	-	Hap(36) Dis(72) Fea(16) Ang(8) Sur(89) Sad(13) Oth(66)	17	https://github.com/benxianyeteam/MMEW-Dataset
4DME [28]	2022	65	Y	1068	1,200 × 1,600	60 fps	4D	Basler avA1600 65k camera	Pos(34) Neg(127) Sur(30) Rep(6) PosSur(13) NegSur(8)	22	Contact: xiaobai.li@oulu.fi
					640 × 480	60 fps	Grayscale	Stingray F-046B camera	RepSur(3) PosRep(8) NegRep(7) Oth(31)		
					640 × 480	30 fps	RGB	Kinect			
					640 × 480	30 fps	Depth	Xbox 360 camera			
CAS(ME) ³ [17]	2022	247	N	1109	1,280 × 720	30 fps	RGB	Intel® RealSense™ D415 camera	Part A: Hap(64) Dis(281) Fea(93) Ang(70) Sur(201) Sad(64)	ALLE	http://casme.psych.ac.cn/casme/c4
							Depth		Oth(170)		
							PPG		Part C: Pos(16) Neg(99) Sur(30) Oth(20)		
							RSP				
							EDA				
							ECG				
DFME [19]	2023	671	N	7,526	1,024 × 768	200/300/500 fps	RGB	Self-developed high-speed camera	Hap(992) Dis(2528) Fea(892) Ang(619) Sur(1208) Sad(635) Oth(251)	22	https://mea-lab-421.github.io
							EEG	XIMEA MQ022CG-CM camera			
MMME (Ours)	2025	75	N	2,890 trials	24 bits	1,000 Hz	EEG	Neuroscan SynAmps RT EEG system	Hap(92) Dis(163) Fea(124) Ang(50) Sur(105) Sad(55) Con(45)	21	https://github.com/Mac0504/MMME
							PPG		Valence and Arousal		
							RSP				
							SKT				
							EDA				
ECG											

¹ **Year:** The publication year of the dataset's corresponding paper.

² **Num:** The number of participants and micro-expression samples is based on the original paper and the downloaded dataset. Note that not all participants successfully exhibited MEs.

³ **Eth:** Indicates whether the dataset includes participants from multiple ethnic backgrounds. Y: Yes; N: No.

⁴ **Resolution:** For cameras, resolution refers to the number of pixels in captured images, which indicates the clarity or level of detail. For physiological signal acquisition devices, resolution represents the smallest distinguishable unit of signal, typically measured in bits.

⁵ **Sampling rate:** The camera's sampling rate is measured in frames per second (fps), while the sampling rate for physiological signals is measured in Hz.

⁶ **Modality:** HS-RGB denotes 2D high-speed video; NIR denotes 2D near-infrared video; Grayscale denotes grayscale video; 4D denotes dynamic 3D video; Depth denotes depth images; PPG represents photoplethysmography; RSP represents respiratory signals; EDA represents electrodermal activity; ECG represents electrocardiograms; and EEG represents electroencephalograms.

⁷ **Emotion:** Pos: Positive; Neg: Negative; Sur: Surprise; Amu: Amusement; Hap: Happiness; Dis: Disgust; Rep: Repression; Fea: Fear; Ang: Anger; Con: Contempt; Sad: Sadness; Ten: Tense; PosSur: Positively Surprise; NegSur: Negatively Surprise; RepSur: Repressed Surprise; PosRep: Positively Repression; NegRep: Negatively Repression; Oth: Others; Unc: Unclear.

⁸ **AU:** ALL: all observed AUs; ALLE: all observed AUs except eye blinking.

⁹ The '-' in the table indicates that the information is not provided in the original paper.

2. Related Work

2.1. ME Databases

The advancement of ME analysis technology relies heavily on the availability of spontaneous ME datasets. In recent years, growing interest in MEs within affective computing, combined with an increasing demand for advanced ME analysis, has driven the meticulous development and public release of several ME datasets. Table 1 offers a detailed overview of these datasets' key features, including release

year, participant numbers, sample characteristics, acquisition equipment, annotation details, and accessible download links. The following analysis assesses these datasets in terms of paradigm design, experimental conditions, data modalities, and sample annotation practices.

2.1.1. Paradigm Design

Early ME samples were derived from posed, non-spontaneous datasets, such as the Polikovskiy database (2009) [29] and the USF-HD dataset (2011) [30], where participants

were instructed to mimic rapid facial expressions. However, these posed MEs failed to capture participants' authentic emotional states and diverge from the involuntary nature of MEs observed in natural contexts. Consequently, such databases have seen limited application in contemporary ME research. According to the emotional leakage theory [31], when individuals suppress their emotions to maintain a neutral facade, brief, involuntary facial muscle movements—known as MEs—may emerge, inadvertently revealing the concealed affective states. Building on this insight, researchers have refined experimental approaches by introducing the neutral face paradigm [27] to elicit spontaneous MEs. In this method, participants are instructed to inhibit facial movements and preserve a neutral expression while viewing emotionally evocative videos. Owing to its controlled environment and practical feasibility, this paradigm has been widely embraced by spontaneous ME datasets, such as SMIC (2011) [21], CASME (2013) [22], CASME II (2014) [23], SAMM (2016) [24], CAS(ME)² (2017) [26], MMEW (2021) [27], 4DME (2022) [28], and DFME (2023) [19]. Nonetheless, the laboratory-based neutral paradigm differs from real-world conditions, where MEs typically manifest during interpersonal interactions, and individuals may conceal true emotions not only by maintaining neutrality but also by displaying expressions opposite to their genuine feelings or simply smiling.

Recognizing that social interactions elicit more diverse expressions than solitary settings, the MEVIEW dataset [25] compiled video footage from online sources, such as poker games and television interviews, to capture MEs in genuine interactions. Yet, frequent camera movements and angle switches result in fewer samples with complete facial views in this dataset. To enhance ecological validity, the CAS(ME)³ (2022) [17] was constructed in a controlled experimental environment using high-risk simulated crime scenarios to elicit MEs. Researchers evaluated participants' deceptive behaviors during the interrogation phase. However, MEs elicited under this paradigm remain closely linked to deceptive behavior, and their faint signals were often obscured by non-emotional facial movements inherent to dialogue. Based on the neutral facial paradigm, this study developed a Continuous Monitoring and Real-time Reminder (CMRR) experimental paradigm to enhance participants' motivation for facial expression suppression, as analyzed in Section 3.3.

2.1.2. Experimental Equipments

In terms of experimental equipment, capturing MEs imposes stringent technical demands on imaging devices. Due to the brief duration and low intensity of MEs, high-frame-rate and high-resolution cameras are essential to accurately record subtle changes in facial muscle activity [32]. However, early MEs datasets were constrained by the limited performance of their recording equipment, with frame rates typically below 100 frames per second (fps) and resolutions often restricted to 640×480 pixels. Specifically, in the first publicly available spontaneous MEs database, SMIC, the HS

subset was recorded using a 100 fps camera, while the VIS subset was captured at a mere 25 fps. Similarly, datasets such as MEVIEW, 4DME, CAS(ME)², and CAS(ME)³ employed a sampling rate of 30 fps, while CASME used 60 fps and MMEW utilized 90 fps. Notably, at a frame rate of 30 fps, a complete MEs sample captures a maximum of 15 frames, resulting in a relatively coarse retention of temporal variation characteristics [33]. To address these limitations and enhance data quality, subsequent studies have adopted higher-performance industrial-grade cameras. For instance, CASME II employed a Point Grey camera with a frame rate of 200 fps, and the SAMM dataset utilized a 200 fps Basler Ace camera. Particularly noteworthy is the DFME dataset, where the research team developed a custom high-speed camera with a configurable frame rate, achieving a maximum sampling speed of 500 fps. Regarding resolution, the lowest in existing public datasets is SMIC's 640×480 pixels, while the highest reaches $2,040 \times 1,080$ pixels in the SAMM dataset. Although high frame rates and resolutions significantly improve the precision of MEs capture, excessively high parameter settings may introduce challenges such as data redundancy, increased transmission bandwidth demands, and elevated storage and processing burdens. Consequently, researchers must strike a balance between accurate capture and data processing efficiency during experimental design to ensure both the quality of MEs data and the feasibility of experimentation. In the configuration of lighting environments, stable and appropriate illumination conditions play a critical role in determining the quality of MEs data collection. To mitigate image flickering caused by 50 Hz alternating current, studies have predominantly adopted direct current (DC)-powered LED lighting systems. To ensure uniform light distribution across the participant's facial region, experiments typically combine LED lights with umbrella reflectors. Furthermore, to minimize background interference in micro-expression recognition (MER), experimental setups often incorporate plain-colored backdrops. This facilitates precise facial region segmentation and feature extraction during subsequent image processing stages. In accordance with the aforementioned experimental environment configuration, this study employed an XIMEA industrial-grade high-speed camera for facial image acquisition, with a capture resolution of $2,040 \times 1,080$ pixels and a frame rate of 150 fps. To ensure reliable storage of the substantial volume of data, the experimental system was equipped with a 100TB disk array storage device. The detailed configuration of experimental equipment is presented in Section 3.1.

2.1.3. Data Modalities

ME analysis is a prominent computer vision task, typically performed using facial images or videos. Li *et al.* [28] argued that existing ME datasets suffer from a lack of data diversity, and the monotonous data formats restrict the application of current MER methods. Zhao *et al.* [34] proposed that investigating the neural mechanisms underlying MEs could lay the foundation for MER based on PS, thereby helping to

overcome the limitations of MER and broaden its application scenarios. Li *et al.* [5] further suggested that utilizing multiple modalities could provide complementary information and enhance classification robustness. For example, different emotional expressions can produce distinct changes in autonomic nervous system activity, such as increased heart rate and decreased skin temperature during fear. Therefore, PS can be employed to integrate complementary information for further improving MER. Recent advancements have seen the inclusion of additional modalities in ME datasets. For instance, the SMIC dataset incorporates both RGB and near-infrared (NIR) images to increase data diversity. Experimental results demonstrate that under low-light conditions, the NIR camera exhibits a clear advantage over conventional cameras. The 4DME dataset features RGB images, grayscale images, depth images, and dynamic 3D videos (referred to as 4D) [35], providing richer data that helps mitigate the noise issues typical in traditional 2D videos, such as those caused by self-occlusion, head movement, and lighting variations. Experimental findings suggest that 4D data offers potential advantages in MER tasks, with the integration of information from multiple views proving more effective than relying on any single view. The CAS(ME)³ dataset includes visual information, PS, and speech signals. Experimental results indicate that depth information, as an additional modality, effectively enhances the feature extraction of ME. However, the recognition performance when incorporating EDA or speech signals did not meet expectations. This may be due to insufficient signal denoising and filtering, as well as the inability of speech signals to adequately capture the characteristics of MEs.

It is important to note that different modalities often have varying sampling frequencies, making data synchronization a critical step in multimodal fusion research. Due to technical limitations, the SMIC dataset exhibits a time delay of approximately 3–5 s between the starting points of the three cameras, requiring manual synchronization during post-processing. In contrast, the CAS(ME)³ dataset employs an Intel® RealSense™ D415 camera to simultaneously record RGB color images and their corresponding depth information, while physiological signals are collected using a BIOPAC MP160 multi-channel physiological recorder. However, the associated publications on this dataset do not explicitly specify the precise synchronization method between physiological and speech signals and the video data. The 4DME dataset, on the other hand, achieves data synchronization across all cameras using a trigger mechanism integrated into its audio capture system. In this study, a shared trigger between the camera and the BIOPAC system was employed to generate timestamps, ensuring precise synchronization between facial image capture and PS acquisition.

2.1.4. Sample Annotation

As a crucial step in the construction of ME datasets, precise and scientifically rigorous sample annotation provides reliable classification labels for ME analysis models. The annotation process typically requires multiple professionally

trained Facial Action Coding System (FACS) coders to analyze video frames sequentially, identifying the occurrence and duration of facial action units (AUs). The final emotion labels for MEs are then determined by integrating three key sources of information: AU annotations, the emotional category of the elicitation materials, and participants' self-reported emotions.

In the annotation methods used for ME datasets, two primary labeling systems are commonly adopted: discrete emotion models and continuous emotion models. Regarding discrete annotation methods, several well-known datasets employ different classification standards. Notably, SMIC, CAS(ME)², CAS(ME)³, and 4DME utilize a three-class classification scheme, categorizing samples into positive, negative, and surprise. This simplified classification strategy not only reduces annotation complexity but also mitigates the issue of class imbalance. To enhance the accuracy of emotion analysis, datasets such as CASME, SMM, MEVIEW, MMEW, CAS(ME)³, and DFME adopt a more detailed seven-class system based on Ekman's basic emotion theory, classifying emotions into happiness, disgust, fear, anger, surprise, sadness, and others. In contrast to discrete annotation methods, continuous emotion models represent emotional states as coordinate points in a multi-dimensional space. Specifically, this model constructs a two-dimensional coordinate system comprising valence and arousal, where valence reflects the positive or negative nature of an emotion, while arousal represents variations in energy levels from calmness to excitement. Although the SMM dataset recorded valence and arousal data during experiments, these continuous dimension annotations were not included in the final annotation files. Recognizing the advantages of continuous emotion models in quantifying emotional intensity and their applicability in continuous emotion estimation tasks, the ME dataset constructed in this study integrates both annotation systems. It provides not only traditional discrete emotion labels but also valence and arousal annotations, thereby offering a more comprehensive and fine-grained representation of emotions.

2.2. ME Analysis Methods

2.2.1. ME Recognition Methods

MER involves identifying emotions conveyed through brief and subtle facial expressions, playing a vital role in affective computing by revealing genuine human emotions. In recent years, the release of publicly available ME datasets has significantly fueled the advancement of automated ME recognition (MER) techniques based on computer vision.

MER based on visual information. ME feature extraction techniques have evolved from early handcrafted computer vision methods to contemporary deep learning approaches, broadly classified into spatial and temporal strategies. In terms of spatial feature extraction, a common approach involves segmenting regions of interest (ROIs) on the face based on the FACS [36]. This method divides the face into multiple regions corresponding to independent muscle

groups, followed by appearance normalization for each region [37–39]. Polikovskiy et al. [29] proposed a gradient-based feature that constructs histograms of gradient projections in local regions to describe spatial characteristics. Similarly, the Local Binary Pattern (LBP) [40] operator robustly captures local appearance features by comparing the relative brightness of neighboring pixels [21]. In the realm of deep learning, convolutional and pooling layers are employed to extract spatial features, while recent advancements incorporate attention mechanisms to enhance the network’s ability to focus on critical regions by generating weighted feature map masks. Additionally, Graph Convolutional Networks (GCNs) model facial AUs as graph nodes, further optimizing spatial feature extraction by leveraging prior knowledge to improve performance [41]. Given the transient and spontaneous nature of MEs, temporal feature extraction is equally critical. Traditional handcrafted feature methods often treat video data as three-dimensional spatio-temporal volumes, applying feature extraction operators, such as LBP-TOP [42] and 3DHOG [29], across sections encompassing both spatial and temporal dimensions. Optical flow-based features achieve similar objectives by integrating local spatial and temporal information [43, 44]. In deep learning approaches, preprocessed optical flow matrices are commonly used as input instead of raw images to capture temporally proximate information [45, 46]. To model longer-term temporal dependencies, some studies treat video sequences as three-dimensional matrices or employ Recurrent Neural Networks (RNNs) and Long Short-Term Memory (LSTM) networks for temporal modeling [47, 48]. These approaches significantly enhance the robustness and accuracy of ME feature extraction.

MER based on multi-modal fusion. Benlamine *et al.* [49] captured MEs and corresponding EEG signals from participants viewing image stimuli, employing time- and frequency-domain features of 1 s EEG signals to train machine learning algorithms for MER. Kim *et al.* [50] classified discrete emotions in MEs using EEG and facial electromyography (EMG) signals, offering electrode placement guidelines for designing wearable MER devices. Saffaryazdi *et al.* [51] integrated EEG, GSR, and PPG to detect emotions in MEs, demonstrating that combining MEs with brain and peripheral physiological signals enhances the reliability of detecting underlying emotions, underscoring the distinct advantage of MEs over MaEs in revealing authentic emotions. Zhao *et al.* [52] utilized EEG to investigate the reorganization of functional brain networks during MEs, aiming to uncover neural mechanisms that could provide electrophysiological indicators for MER. Their findings revealed that during MEs, participants exhibited higher global and nodal efficiency in the frontal, occipital, and temporal regions, confirming the possibility of using EEG to recognize MEs. Furthermore, they conducted an EEG study on the differences in brain activation between MEs and MaEs, exploring the neural mechanisms underlying MEs and their distinctions from MaEs from a neuroscience perspective [53]. The results showed that under positive emotions, MEs significantly

activated the premotor cortex, supplementary motor cortex, and middle frontal gyrus, providing a theoretical foundation for multimodal MER.

2.2.2. ME Spotting Methods

The objective of ME spotting is to precisely identify the onset, apex and offset frames of MEs in video sequences. However, the transient and subtle nature of MEs presents substantial challenges for precise keyframe localization, resulting in poor performance of vision-based spotting algorithms and difficulty meeting practical requirements.

ME Spotting based on visual information. ME spotting methods based on visual information primarily involve two approaches: handcrafted feature-based and deep learning-based. Handcrafted-based methods typically rely on detailed feature engineering and signal processing design. These approaches extract features such as LBP, HOG, HOOOF and MDMO. They identify the frame with the highest feature magnitude as the apex frame or determine the expression interval using threshold strategies. For instance, Han *et al.* [54] combined LBP and MDMO to extract more robust features, where LBP captures texture information, and MDMO detects motion features by identifying the dominant direction in optical flow histograms. Esmaeili *et al.* [55] developed an enhanced LBP descriptor that computes LBP across fifteen planes to capture critical information related to MEs. Although this approach achieved promising results, it is computationally intensive and time-consuming. More recently, Ma *et al.* [56] introduced a feature extraction method based on the Regional Histogram of Oriented Optical Flow (RHOOOF) to automatically detect apex frames, achieving robust results. However, since handcrafted feature methods heavily depend on manually designed feature extractors, they require extensive expertise and involve complex parameter tuning processes. With the rapid development of deep learning technologies, several well-designed network architectures, such as AlexNet [57], ResNet [58], and Long Short-Term Memory (LSTM) networks [59], have gradually been applied to ME Spotting. These approaches, which leverage the advantages of automated feature engineering and end-to-end training, are becoming mainstream in the field. Zhang *et al.* [60] were the first to introduce deep learning into ME Spotting. They used Convolutional Neural Networks (CNNs) to extract deep features and proposed a feature matrix processing method to search for apex frames from long video sequences. Verburg *et al.* [61] were the first to apply RNNs to ME Spotting. Their method extracts HOOOF features from sliding windows and inputs these features into an RNN composed of LSTM units for classification. However, the brief duration and subtle intensity of MEs continue to pose challenges for improving the accuracy and robustness of deep learning frameworks.

ME spotting based on multi-modal fusion. When individuals experience intense emotions, sympathetic nervous system activity is expected to increase. During such moments, MEs may briefly appear, accompanied by changes in ECG signals, such as fluctuations in heart rate (HR)

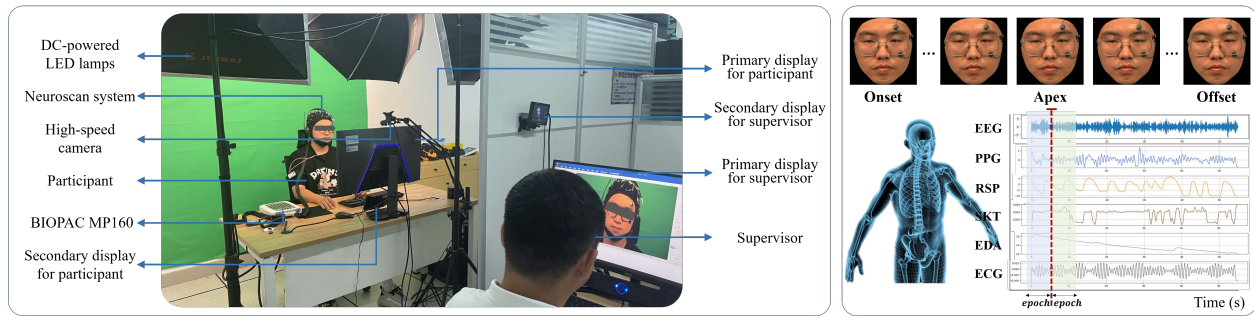


Figure 2: Experimental setup and signal examples of the MMME dataset acquisition system. The left panel depicts the laboratory environment, including the participant and data acquisition equipment. The right panel presents representative samples of the collected multimodal data, featuring key frames of ME and time-series representations of multiple PS.

[62]. MEs and HR variations represent external behavioral expressions and internal physiological responses to emotions, respectively, both influenced by emotional triggers and regulatory mechanisms. Early research estimated HR from facial videos by analyzing subtle color changes and micro-movements caused by cardiovascular pulsations. For example, Gupta *et al.* [63] investigated the feasibility of using estimated instantaneous HR fluctuations to identify MEs. Their findings revealed that HR fluctuation amplitudes significantly increased during the occurrence of MEs. Building on this insight, they used variations in instantaneous HR to distinguish genuine ME intervals from the plausible ME intervals. Similarly, Zhang *et al.* [64] detected participants' HR from ME videos and developed a spatiotemporal fusion network incorporating HR information. Their results demonstrated that integrating image data with HR signals via a multimodal learning approach provides a more comprehensive representation of ME features. Additionally, Setyaningrum *et al.* [65] conducted real-time detection of MEs and HR from facial videos to explore their relationship. Using Eulerian Video Magnification (EVM) [66] and Fast Fourier Transform (FFT) [67] for HR detection, they found that emotions reflected by MEs influenced HR: angry expressions corresponded to higher HRs, sad expressions to lower HRs, and happy expressions exhibited greater variability. Despite these advancements, most studies estimated HR fluctuations from facial videos, which are susceptible to environmental disturbances. To address this limitation, Zou *et al.* [68] collected facial MEs and ECG signals, and their statistical analysis revealed a significant correlation between MEs and the time-domain features of heart rate variability (HRV). However, their study did not extend to leveraging HRV for the recognition or spotting of MEs.

3. MMME Database Profile

In this study, we developed a comprehensive multimodal ME dataset, named MMME, which synchronously captures facial action signals (MEs), central nervous system signals (EEG), and multiple peripheral physiological signals (PERIPS) including PPG, RSP, SKT, EDA, and ECG. These modalities serve as reliable indicators of emotional states,

providing robust data support for exploring the integration of multi-source data to enhance the performance of emotion recognition tasks. Each sample was meticulously annotated with facial AUs and emotion category labels. Furthermore, considering the co-occurrence of MEs and macro-expressions (MaEs) during video viewing by participants, the MMME dataset also systematically collected and annotated MaEs, thereby enriching the dataset's diversity and offering a more comprehensive foundation for research on emotional representation. The following sections detail the dataset construction process, including participants and experiments, emotion elicitation materials, experimental paradigm, annotation methods, and statistical analysis of the collected samples.

3.1. Participants and Equipments

In this study, we recruited a total of 75 participants, including 44 males and 31 females, with ages ranging from 21 to 40 years. The average age was 28.80 years (standard deviation = 4.55). All participants were right-handed, had normal or corrected vision, had no history of mental illness, and were not at risk for depression. Prior to the experiment, all participants provided written informed consent and consented to the use of their likeness. Each participant exhibited at least one ME in the video clips.

The experimental setup, as illustrated in the left panel of Fig. 2, was conducted in a controlled environment. To eliminate 50 Hz AC-induced flickering, we implemented a specialized lighting system consisting of three 600-watt DC-powered LED lights equipped with umbrella reflectors. These lights were strategically positioned to focus illumination on the participant's face, ensuring consistent and high-intensity lighting conditions. Specifically, the lighting configuration comprised one central light positioned directly in front of the participant and two additional lights placed at 45 angles to the left and right of the participant. Participants were seated one meter from the main display monitor, with a green background panel positioned behind them to facilitate subsequent facial image processing. The participants' facial images were acquired using a high-speed camera system (XIMEA MQ022CG-CM, Germany) equipped with an industrial lens (KOWA LM16JC10M, 16 mm focal length,

Japan) operating at 150 fps with a resolution of $2,040 \times 1,080$ pixels. The camera was positioned above the main display, maintaining direct alignment with participants' facial orientation. Neural activity was recorded through a 64-channel QuickCap coupled with the Neuroscan SynAmps RT system, acquiring EEG data at 1000 Hz. Concurrently, PERI-PS were captured using the BIOPAC MP160 acquisition system and AcqKnowledge 5 software (BIOPAC Systems, Inc., USA) at an identical sampling rate of 1000 Hz. For ECG recording, Ag/AgCl disposable vinyl electrodes (EL503; BIOPAC Systems, Inc.) and conductive gel were used to collect signals in a lead II configuration. EDA data were collected from the inner phalanges of the index and middle fingers of the left hand. A shared trigger between the camera, Neuroscan, and BIOPAC system was employed to generate timestamps, ensuring precise synchronization between facial image capture and physiological signal acquisition.

3.2. Emotion Elicitation Materials

Given that video stimuli containing both visual and auditory elements can effectively elicit significant emotional states and physiological responses in participants within laboratory settings [69], we curated a dataset of 320 video clips from online sources to construct an emotion-inducing stimulus library. To ensure the immediacy and intensity of emotional responses, each clip was edited to a duration of no more than one minute. These videos were designed to evoke seven distinct emotions: happiness, surprise, sadness, fear, anger, disgust, and contempt. These emotions are considered to be universal, independent of cultural, historical, or individual differences, and are typically expressed in a similar manner across individuals. To assess the effectiveness of these videos in eliciting emotions, we recruited 20 independent evaluators to watch and rate the clips. After viewing randomly presented clips, the evaluators completed a questionnaire based on a nine-point Likert scale [70], rating each video according to three criteria: arousal, valence, and emotion category. Notably, these evaluators did not participate in the subsequent emotion induction experiment to prevent potential bias. Conducting a reliability assessment of the questionnaire is a crucial step in ensuring data quality and enhancing the reliability and validity of research conclusions. We utilized Cronbach's alpha coefficient [71] to assess the internal consistency of the questionnaire results, defined as follows:

$$\alpha = \frac{n}{n-1} \left(1 - \frac{\sum s_i^2}{s_T^2} \right), \quad (1)$$

where n is the number of items, s_i^2 is the variance of the i^{th} item, and s_T^2 is the variance of the total scores. The calculated Cronbach's alpha coefficients for the questionnaire exceeded 0.80, indicating good internal consistency and trustworthiness of the results.

Furthermore, we employed the Intraclass Correlation Coefficient (ICC) [72] to assess consistency, which is a

widely used reliability metric in the analysis of assessor reliability. The formula is as follows:

$$\rho = \frac{MS_r - MS_e}{MS_r + (n-1)MS_e}, \quad (2)$$

where MS_r is the mean square between subjects, MS_e is the mean square error, and n is the number of subjects. At a 95% confidence interval, the ICC coefficients for pleasure and arousal were 0.768 and 0.697, respectively, indicating good consistency for both dimensions.

Based on the evaluation results, we ultimately selected six representative video clips for each emotional category, resulting in a total of 42 video stimuli being utilized in the experiment. These carefully curated video materials contain intensive stimulation points with high arousal potential, effectively eliciting singular target emotions.

3.3. Experimental Paradigm

To familiarize participants with the experimental procedure, a pre-experiment was conducted prior to the formal experiment. The videos used in the pre-experiment were not repeated in the formal experiment, and the data collected during the pre-experiment were not included in the final analysis. In the formal experiment, participants controlled the playback of the video clips by pressing the space bar, with each clip lasting approximately 60 s. After each video segment, participants were required to quickly and accurately report the type of emotion, emotional valence, and arousal level within 25 s. A 30 s neutral video was then played to help participants relax. This sequence constituted a complete trial. Our experiment included a total of 42 trials, meaning each participant watched 42 video clips. Throughout the experiment, facial videos and various physiological signals were recorded simultaneously. Additionally, participants were instructed to minimize head and body movements as much as possible. Fig. 3 provides a detailed overview of the experimental process.

Unlike traditional "immersive emotion induction" paradigms, this study aims to establish an experimental environment specifically tailored for ME research. Given the

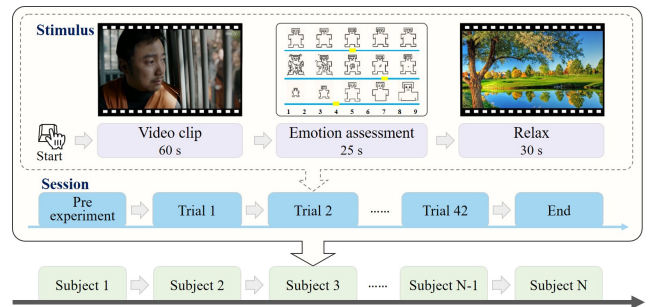


Figure 3: The detail of the experimental procedure. Our experiment included a total of 42 trials. Throughout the experiment, facial videos and various physiological signals were recorded simultaneously.

Table 2

The list of AU codes involved in MEs in the MMME dataset, along with their corresponding action descriptions, occurrence regions, and counts

AUs	Action description	Region	Count	AUs	Action description	Region	Count	AUs	Action description	Region	Count
AU1	Inner Brow Raiser	Upper	54	AU10	Upper Lip Raiser	Mid	33	AU17	Chin Raiser	Lower	39
AU2	Outer Brow Raiser	Upper	24	AU11	Nasolabial Deepener	Mid	6	AU18	Lip Puckerer	Lower	8
AU4	Brow Lowerer	Upper	357	AU12	Lip Corner Puller	Mid	48	AU20	Lip stretcher	Lower	15
AU5	Upper Lid Raiser	Mid	12	AU13	Cheek Puffer	Lower	12	AU25	Lips parted	Lower	12
AU6	Cheek Raiser	Upper	17	AU14	Dimpler	Lower	165	AU26	Jaw Drop	Lower	10
AU7	Lid Tightener	Mid	54	AU15	Lip Corner Depressor	Lower	23	AU41	Lid droop	Mid	11
AU9	Nose Wrinkler	Mid	12	AU16	Lower Lip Depressor	Lower	16	AU42	Slit	Upper	8

¹ Upper: the upper face; Mid: the mid-face; Lower: the lower face.

intrinsic nature of MEs as “suppressed-leakage” phenomena [73], it is essential to maintain a moderate level of facial control pressure throughout the experiment. Although the classic ME elicitation paradigm instructs participants prior to the experiment to suppress facial expressions and minimize bodily movements [23, 26], our observations revealed that participants still exhibited “uncontrolled” behaviors, such as unconscious relaxation of facial control and frequent head or body movements. Notably, these phenomena persisted despite participants being informed that such behaviors would result in a reduction of their compensation, and they often required considerable time to return to the required suppression state. This finding suggests that pre-experimental instructions and intrinsic motivation alone are insufficient to ensure consistent experimental conditions.

To address this issue, we developed the Continuous Monitoring and Real-time Reminding (CMRR) paradigm, in which the experimenter continuously monitors participants’ facial expressions and body movements in real time. When a participant exhibits signs of facial relaxation or frequent head and body movements, the experimenter triggers a visual prompt on a small auxiliary display. This prompt serves as an immediate signal for the participant to swiftly restore the required level of facial suppression. Experimental results demonstrate that the CMRR paradigm not only accelerates participants’ recovery to the required state but also significantly enhances their ability to maintain this state in subsequent trials. From a theoretical perspective, the CMRR paradigm aligns closely with the core feature of MEs as “emotional leakage within a controlled environment” [27]. In contrast to fully immersive paradigms, CMRR achieves a balance between experimental control and ecological validity by minimizing interference—cues are triggered only when necessary.

3.4. ME Annotation

Following the completion of 2,814 trials and the collection of nearly 80 hours of multimodal emotional data, we rigorously adhered to the annotation protocols established by authoritative ME datasets, such as the CASME series [17, 22, 23, 26]. The annotation of ME samples was conducted independently by two certified experts in the FACS. Using a custom-developed annotation software, the experts analyzed each video frame by frame to precisely

identify the onset, apex, and offset frames of each expression sequence. In this study, facial expressions meeting either of the following criteria were classified as ME samples: (1) total duration from onset to offset not exceeding 500 ms, or (2) duration from onset to apex frame not exceeding 250 ms. Each identified ME sample was subsequently annotated with corresponding AUs and categorized into one of seven basic emotion categories: *happiness*, *surprise*, *sadness*, *fear*, *anger*, *disgust*, or *contempt*. Furthermore, to assess inter-coder reliability, we calculated consistency score (r) between the two annotators, with the computational methodology detailed as follows:

$$r = 2 \times \frac{AU(A_1) \cap AU(A_2)}{All_{AU}}, \quad (3)$$

where $AU(A_1) \cap AU(A_2)$ is the number of AUs both annotators agreed, and All_{AU} is the total number of AUs in an ME labeled out by the two annotators. In this study, the inter-annotator reliability score was 0.84, which is comparable to those reported for the CAS(ME)² (0.82) [26] and DFME (0.83) [19] datasets. Ultimately, through comprehensive discussions, the annotators reached a consensus, producing a consistent and reliable set of annotations.

Drawing upon commonly observed AU patterns in published ME datasets and considering participants’ actual performance, we annotated a total of 21 distinct AU categories. These AUs were distributed across facial regions as follows: 5 categories in the upper face (from hairline to below eyebrows), 7 categories in the mid-face (from below eyebrows to nasal base), and 9 categories in the lower face (from nasal base to chin). Table 2 presents a detailed list of AU codes, along with their corresponding facial action descriptions, regions, and counts. It can be observed that the three most frequently occurring AUs are AU1 (Inner Brow Raiser), AU2 (Outer Brow Raiser), and AU12 (Lip Corner Puller). These AUs are primarily located in facial regions most relevant to MEs: the eyebrows and the corners of the mouth, which are critical for ME analysis.

After meticulous annotation, we obtained 634 MEs (mean duration = 389 ms, SD = 97 ms), 2841 MaEs (mean duration = 1634 ms, SD = 328 ms) and multimodal physiological data for 4,200 trials. Fig. 4 illustrates representative

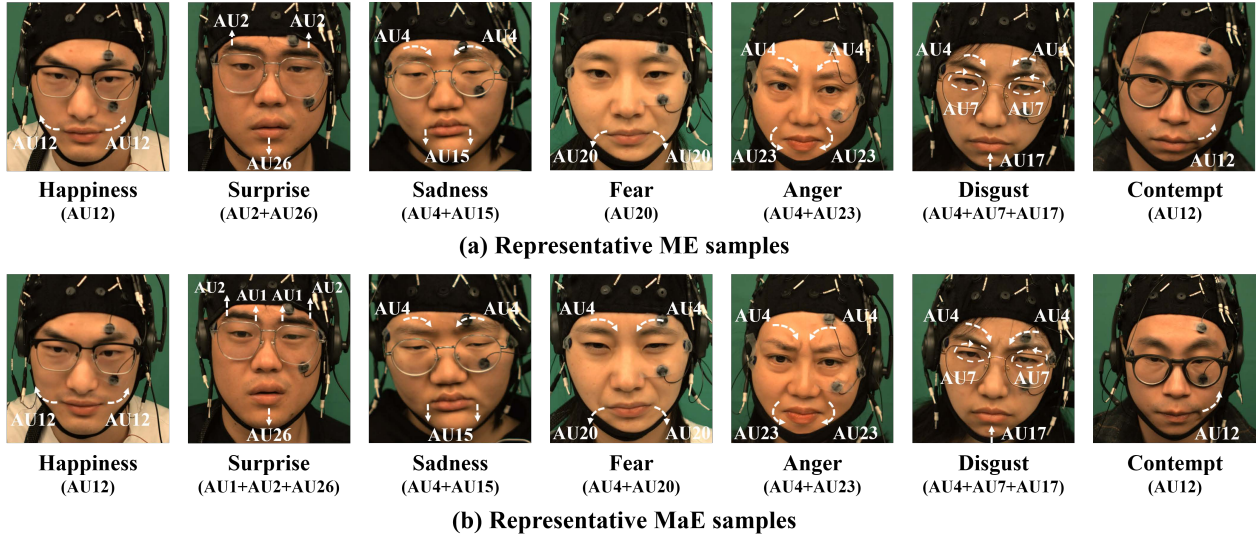


Figure 4: Representative ME and MaE samples for seven emotion categories in MMME. White arrows indicate the locations and movement patterns of key AUs, and the circular arrows in the eyelid region indicate the orbital narrowing motion caused by the contraction of the orbicularis oculi muscle.

samples of MEs and MaEs across seven emotion categories in our MMME dataset, accompanied by their corresponding AUs. As shown, MEs are notably more subtle than MaEs, rendering their detection and recognition considerably more challenging. It is worth noting that, the MaEs collected in our dataset demonstrate greater restraint, characterized by reduced motion amplitudes and shorter durations, when compared to those in datasets obtained through emotion-elicitation paradigms (*e.g.*, FER+ [74], BP4D+ [75], CK+ [76]). This distinction arises from the neutral paradigm employed in our study, where participants were explicitly instructed to suppress facial movements during data collection. This unique feature of the dataset offers significant value for investigating facial expressions under suppression, particularly in scenarios or cultural contexts where subtle or restrained emotional expression is prevalent.

3.5. Data Statistics and Analysis

In this section, we perform a statistical analysis of the annotated samples. The results, presented in Fig. 5, highlight four key characteristics: (a) the distribution of seven basic discrete emotions; (b) the distribution of three composite emotions (“Negative,” “Positive,” and “Surprise”); (c) the dataset size and participant gender composition; and (d) a comparison of mean ME durations and their standard deviations across benchmark datasets. The statistical analysis reveals that the number of ME samples is approximately one-fourth that of MaEs (634 vs. 2,841). This observation underscores the inherent difficulty of eliciting MEs in experimental settings due to their spontaneous and transient nature. Regarding the distribution of emotion categories, a pronounced imbalance is evident—an issue commonly observed in publicly available ME datasets. Specifically, samples corresponding to “Disgust,” “Fear,” and “Surprise” are relatively abundant, whereas those for “Sadness” and

“Contempt” are significantly underrepresented. This disparity may stem from two primary factors: (1) variations in the difficulty of eliciting different emotions in experimental paradigms and (2) differences in the recognition difficulty of specific facial AUs. Notably, among the seven basic emotions, five (“Anger,” “Disgust,” “Fear,” “Sadness,” and “Contempt”) fall under the “Negative” valence category, leading to a predominance of “Negative” samples within the composite emotion distribution. In terms of data modality, the novelty of the MMME dataset lies in its multimodal data acquisition framework, which simultaneously records facial expression videos, central nervous system signals, and peripheral nervous system signals. This comprehensive approach provides a robust foundation for modeling the relationship between facial expressions and neural activity. Duration analysis indicates that the average ME duration in the MMME dataset (381.7 ± 100.5 ms) is consistent with those observed in publicly available datasets such as the CASME series, SAMM, and MMEW. This consistency validates the reliability of our dataset in terms of temporal distribution characteristics. In summary, through its multimodal nature and standardized annotation framework, the MMME dataset not only addresses the limitations of existing unimodal ME datasets but also serves as a crucial experimental platform for investigating the neural mechanisms underlying MEs and advancing their decoding algorithms.

4. Database Evaluation

In this section, we design a series of experimental tasks to evaluate the effectiveness of the MMME dataset, with the task framework illustrated in Fig. 6. The evaluation tasks primarily focus on three aspects: (1) Concordance analysis between MEs and PS, (2) ME recognition (categorized into vision-based methods and multimodal fusion approaches), and (3) ME spotting (similarly divided into two

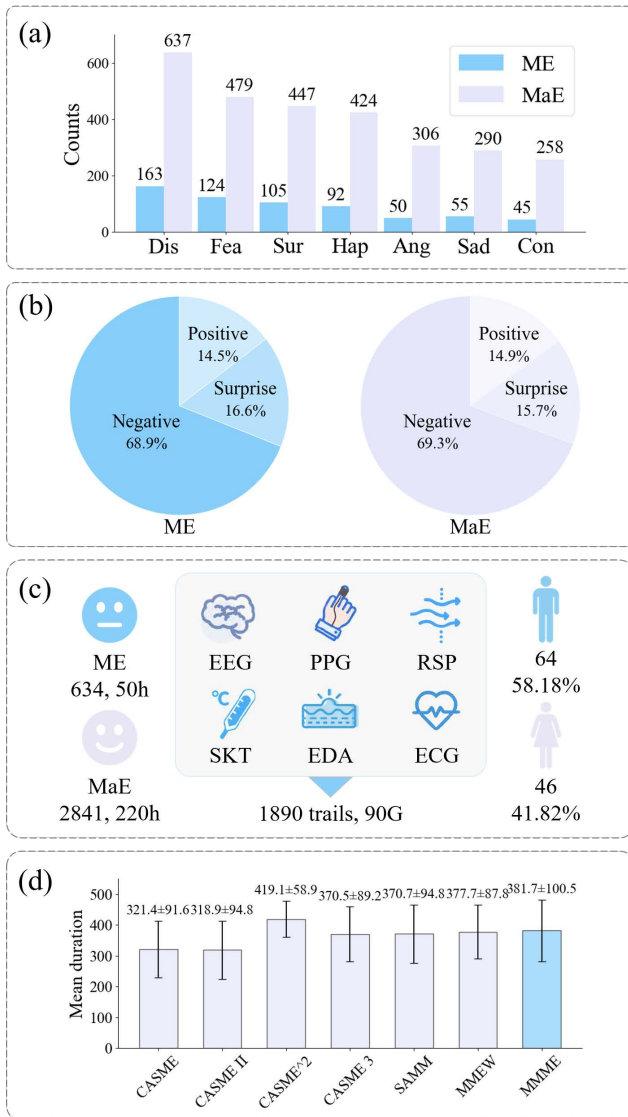


Figure 5: Statistical analysis of annotated samples in the MMME dataset.

approaches). The concordance validation between MEs and PS provides a theoretical foundation for designing fusion strategies, thereby effectively leveraging the complementary advantages across different modalities, as detailed in Section 4.1. Both ME recognition (Section 4.2) and ME spotting (Section 4.3) tasks incorporate unimodal and multimodal analyses, establishing comprehensive benchmarks for dataset validation.

4.1. The Concordance Between MEs and PS

Numerous studies have demonstrated that multimodal fusion techniques offer significant advantages in the field of affective computing, substantially improving the accuracy and robustness of emotion recognition [77–79]. However, research in the specific domain of ME analysis remains predominantly confined to unimodal visual approaches. Notwithstanding this limitation, recent years have witnessed emerging attempts to integrate MEs with physiological

signals to more comprehensively capture subtle emotional variations. For instance, Kim *et al.* [50] successfully classified discrete emotions in facial MEs by fusing EEG and facial EMG data. Saffaryazdi *et al.* [51] employed a multimodal approach incorporating EEG, GSR, and PPG to identify emotions underlying MEs. Furthermore, Zhao *et al.* [53] conducted a focused investigation comparing neural activation patterns between MEs and MaEs using EEG data, revealing differences in brain activity. Despite these pioneering efforts that have expanded the possibilities of multimodal research, they share a common limitation: none have systematically examined the concordance or underlying mechanisms between MEs and multimodal physiological data. This knowledge gap results in a lack of theoretical foundation for multimodal fusion strategies, leaving the complementary advantages among modalities insufficiently explored and utilized. From a neurophysiological perspective, MEs and PS play complementary roles in emotional expression. During intense emotional episodes, MEs reflect transient emotional changes through subtle facial muscle movements, while PS record dynamic activation patterns of the autonomic nervous system. Theoretically, effective integration of these modalities could not only provide a more comprehensive emotional profile by capturing both external behavioral manifestations (MEs) and internal physiological responses, but might also reveal synergistic patterns between them. Such integration would thereby facilitate the development of more precise emotion recognition models.

To optimize the fusion of visual signals and physiological features during ME occurrences, this study explores the concordance and potential interaction mechanisms between MEs and various PERI-PS under high-arousal emotional stimuli. Specifically, we investigated whether these modalities exhibit synchronous variations during emotional responses. Since PERI-PS were continuously recorded while MEs occur sparsely, the apex frames of MEs were utilized to segment the corresponding PS. Considering that physiological responses to emotional stimuli typically exhibit temporal delays, an appropriate redundancy was introduced in the

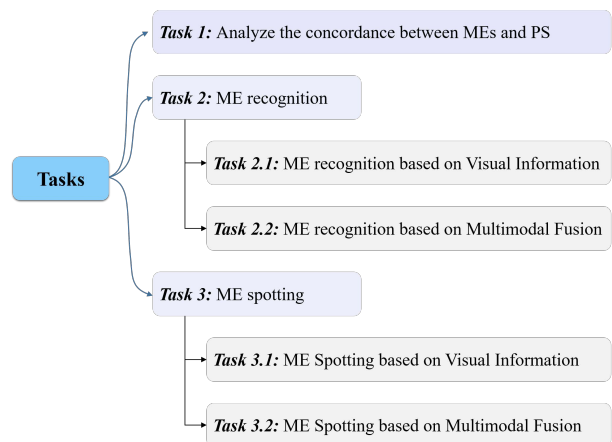


Figure 6: Task framework for dataset evaluation: concordance, recognition, and spotting of MEs.

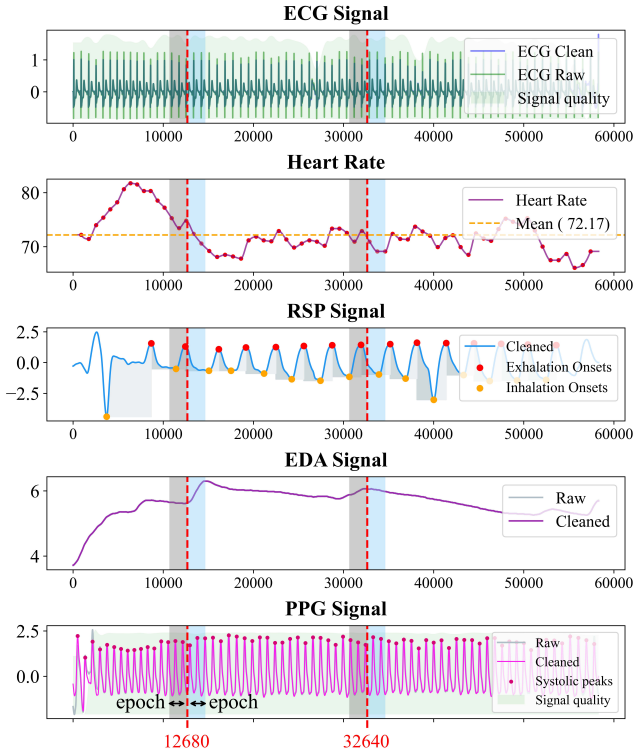


Figure 7: Temporal variations of different PERI-PS in a single trial, where two MEs occur with apex frames at 12,680 ms and 32,640 ms.

signal segmentation process to cover this delay. Research has indicated that emotional fluctuations can be reflected in PERI-PS within a temporal window ranging from 3 to 15 s. For instance, Kim *et al.* [80] performed an emotion induction experiment, simultaneously recording multiple signals, with annotated segments ranging from 3 to 15 s in duration. Other studies [81, 82] have also confirmed durations associated with emotional changes. Therefore, the duration of 3 s and 15 s were chosen to cover the range of 3 to 15 s, and two additional durations (5 s, and 10 s) were also considered in our study. Consequently, this study employed epoch durations of 3, 5, 10, and 15 s centered around the apex frames of MEs for segmentation, while ensuring that no other MEs occurred within the same epoch. The open-source neurophysiological signal processing tool NeuroKit2¹ was utilized for PERI-PS processing and feature extraction.

Fig. 7 illustrates the temporal variations of different PS in a single trial. Vertical red dashed lines indicate the apex frames of two MEs in this trial, occurring at 12,680 ms and 32,640 ms. Gray-shaded regions denote the epochs before the apex frames, and blue-shaded regions represent the epochs after them. By examining significant differences in PERI-PS characteristics between these epochs, we aim to identify potential synchronization between MEs and PS. However, through visual inspection, there were no significant abrupt changes in the amplitude or phase of the signal before and after the occurrence of MEs. Therefore, we

further extracted physiological features to investigate, in a statistically significant manner, whether there is consistency between MEs and PERI-PS features. Table 3 presents the results of paired-sample t-tests, which were conducted to analyze the changes in various PERI-PS features before and after the onset of MEs across different time durations. The statistical measures reported include the mean, standard deviation, t-value, and p-value, with gray-shaded p-values indicating statistical significance at the $p < 0.05$ level.

The results reveal a significant association between the occurrence of MEs and certain physiological features. Specifically, within 3 s epochs, several HRV features showed significant differences, including HRV_MeanNN ($p < 0.01$), HRV_SDS (SD) ($p < 0.01$), HRV_MedianNN ($p < 0.01$), HRV_Prc20NN ($p < 0.01$), HRV_Prc80NN ($p < 0.01$), HRV_MinNN ($p < 0.01$), HRV_MaxNN ($p < 0.05$), and HRV_TINN ($p < 0.05$). In addition, RSP features such as RSP_Std_dev ($p < 0.05$) and RSP_Min_value ($p < 0.05$), as well as EDA features including EDA_Mean ($p < 0.05$) and EDA_Mean_amplitude ($p < 0.05$), also exhibited statistically significant changes. Similarly, within 5 s epochs, significant differences were observed in ECG features (RR_Mean ($p < 0.05$), RR_Std ($p < 0.05$)), HRV features (Heart_Rate_Mean ($p < 0.05$), HRV_MeanNN ($p < 0.05$), HRV_MedianNN ($p < 0.05$), HRV_Prc20NN ($p < 0.05$), HRV_Prc80NN ($p < 0.05$), HRV_MinNN ($p < 0.05$)), RSP features (RSP_Std_dev ($p < 0.01$), RSP_Min_value ($p < 0.01$)), EDA features (EDA_Num_peaks ($p < 0.01$)), and SKT features (SKT_Slope ($p < 0.01$)). Furthermore, several physiological features also showed significant differences before and after the occurrence of MEs in 10 s and 15 s epochs. For 10 s epochs, significant changes were identified in ECG features (RR_Std ($p < 0.05$)), HRV features (Heart_CVNN ($p < 0.05$), Heart_CVSD ($p < 0.05$), Heart_MedianNN ($p < 0.01$), HRV_Prc20NN ($p < 0.05$)), RSP features (RSP_Std_dev ($p < 0.01$), RSP_Median ($p < 0.05$), RSP_Max_value ($p < 0.01$), RSP_Min_value ($p < 0.05$)), EDA features (EDA_Mean ($p < 0.01$), EDA_Max ($p < 0.01$), EDA_Min ($p < 0.01$)), and SKT features (SKT_Max ($p < 0.05$)). Similar patterns were also found in the 15 s epochs. These findings provide evidence of a consistent and significant relationship between MEs and PS, thereby establishing a robust foundation for the proposed multimodal fusion of ME and physiological data in this study.

4.2. ME Recognition Validation

To evaluate the effectiveness of the MMME dataset, we conduct micro-expression recognition (MER) tasks in this study, classifying ME samples into emotion categories using both unimodal (visual-only) and multimodal (visual and physiological signal fusion) approaches. The initial recognition results establish a baseline performance, providing a reference for researchers to compare and assess the efficacy of different methods in future work.

¹<https://neuropsychology.github.io/NeuroKit/>

Table 3
Paired sample t-test before and after the ME apex

Physiological Signals	Epoch Feature Name	3s				5s				10s				15s			
		pre.	aft.	t	p	pre.	aft.	t	p	pre.	aft.	t	p	pre.	aft.	t	p
ECG	ECG_Mean	-0.008 (0.005)	-0.009 (0.006)	1.850	0.065	-0.008 (0.003)	-0.008 (0.004)	0.852	0.395	-0.008 (0.002)	-0.008 (0.002)	0.757	0.450	-0.008 (0.002)	-0.008 (0.001)	0.643	0.521
	ECG_Std	0.145 (0.075)	0.146 (0.076)	-1.356	0.176	0.148 (0.075)	0.148 (0.076)	-1.149	0.252	0.149 (0.076)	0.149 (0.077)	-0.812	0.418	0.152 (0.075)	0.152 (0.076)	-0.726	0.469
	ECG_Max	0.635 (0.289)	0.634 (0.288)	0.612	0.541	0.647 (0.290)	0.647 (0.288)	-0.336	0.737	0.654 (0.299)	0.655 (0.299)	-0.400	0.690	0.670 (0.294)	0.670 (0.292)	0.040	0.968
	ECG_Min	-0.509 (0.324)	-0.510 (0.325)	0.256	0.798	-0.528 (0.329)	-0.529 (0.329)	0.852	0.395	-0.539 (0.329)	-0.539 (0.329)	0.092	0.927	-0.425 (0.210)	-0.401 (0.188)	-2.152	0.035
	ECG_Range	1.145 (0.574)	1.144 (0.571)	0.238	0.812	1.175 (0.581)	1.177 (0.577)	-0.802	0.423	1.194 (0.590)	1.195 (0.589)	-0.267	0.789	1.105 (0.456)	1.081 (0.432)	2.197	0.032
	RR_Mean	-	-	-	-	0.000 (0.000)	0.000 (0.000)	2.195	0.032	0.000 (0.000)	0.000 (0.000)	0.904	0.368	0.000 (0.000)	0.000 (0.000)	2.251	0.028
	RR_Std	-	-	-	-	0.000 (0.000)	0.000 (0.000)	-2.078	0.039	0.000 (0.000)	0.000 (0.000)	-0.852	0.040	0.000 (0.000)	0.000 (0.000)	0.831	0.407
	Heart_Rate_Mean	-	-	-	-	72.461 (6.974)	73.165 (6.649)	-2.324	0.021	72.829 (6.679)	72.894 (6.260)	-0.255	0.799	73.010 (6.926)	73.019 (6.134)	-0.033	0.974
	HRV_MeanNN	834.627 (85.430)	822.013 (79.389)	3.333	0.001	834.898 (76.870)	825.213 (71.876)	2.547	0.012	830.045 (70.871)	828.698 (68.417)	0.424	0.672	828.160 (72.466)	826.619 (65.152)	0.457	0.648
	HRV_SDNN	-	-	-	-	32.823 (26.318)	34.431 (31.447)	-0.704	0.482	41.363 (25.866)	41.264 (23.489)	0.050	0.961	44.098 (24.373)	35.868 (16.187)	2.626	0.011
HRV	HRV_RMSSD	34.649 (31.218)	38.304 (44.704)	-1.116	0.265	38.116 (28.609)	40.339 (34.848)	-0.903	0.367	39.595 (26.227)	41.067 (26.973)	-0.705	0.481	39.235 (30.245)	31.962 (14.419)	2.251	0.028
	HRV_SDS	24.260 (22.159)	41.422 (60.396)	-4.440	0.000	39.640 (30.342)	42.901 (39.090)	-1.190	0.235	40.907 (27.646)	42.594 (28.334)	-0.765	0.445	40.079 (31.186)	32.796 (14.957)	2.195	0.032
	HRV_CVNN	0.030 (0.025)	0.036 (0.054)	-1.785	0.075	0.039 (0.032)	0.042 (0.044)	-1.053	0.293	0.049 (0.028)	0.042 (0.018)	2.169	0.033	0.055 (0.029)	0.045 (0.018)	2.665	0.010
	HRV_CVSD	0.041 (0.035)	0.048 (0.064)	-1.634	0.103	0.045 (0.034)	0.049 (0.048)	-1.233	0.219	0.044 (0.031)	0.039 (0.017)	2.014	0.047	0.049 (0.038)	0.039 (0.015)	2.165	0.034
	HRV_MedianNN	834.733 (85.680)	821.886 (83.234)	3.168	0.002	836.817 (76.884)	827.719 (72.604)	2.416	0.016	837.995 (92.978)	798.168 (92.370)	-2.770	0.007	827.403 (72.934)	826.386 (67.692)	0.304	0.762
	HRV_MadNN	24.070 (23.778)	24.896 (28.482)	-0.423	0.673	26.356 (19.568)	26.604 (20.249)	-0.167	0.867	40.318 (23.713)	39.268 (22.013)	0.569	0.570	43.010 (24.941)	44.374 (23.464)	-0.631	0.529
	HRV_MCVNN	0.029 (0.027)	0.030 (0.037)	-0.781	0.436	0.031 (0.022)	0.032 (0.025)	-0.525	0.600	0.049 (0.028)	0.047 (0.026)	0.600	0.549	0.052 (0.028)	0.053 (0.027)	-0.664	0.508
	HRV_IQRNN	18.524 (16.469)	23.107 (36.879)	-1.966	0.050	35.378 (36.621)	37.476 (46.561)	-0.615	0.539	53.160 (33.479)	51.459 (29.749)	0.687	0.493	57.373 (33.103)	57.560 (29.705)	-0.069	0.945
	HRV_SDRMSSD	0.732 (0.090)	0.742 (0.100)	-1.634	0.103	0.888 (0.242)	0.878 (0.235)	0.557	0.578	1.109 (0.382)	1.067 (0.344)	1.351	0.178	1.189 (0.394)	1.171 (0.321)	0.523	0.602
	HRV_Prc20NN	823.523 (85.214)	808.261 (86.755)	3.445	0.001	813.172 (77.488)	801.512 (82.673)	2.366	0.019	759.933 (90.295)	769.739 (89.623)	-2.464	0.016	793.340 (68.306)	792.313 (62.532)	0.290	0.772
PPG	HRV_Prc80NN	845.751 (86.809)	835.757 (77.662)	2.794	0.006	856.791 (81.853)	847.794 (73.769)	2.439	0.015	862.885 (78.437)	860.680 (74.233)	0.624	0.533	863.771 (81.348)	862.277 (72.718)	0.392	0.696
	HRV_pNN50	10.349 (19.741)	11.131 (20.050)	-0.550	0.583	15.020 (19.105)	13.526 (17.879)	1.153	0.250	16.783 (16.827)	17.017 (16.815)	-0.217	0.828	16.310 (15.612)	18.295 (16.240)	-1.883	0.062
	HRV_pNN20	30.144 (24.957)	30.054 (25.251)	0.046	0.963	42.410 (23.413)	43.705 (22.488)	-0.733	0.464	49.753 (21.426)	52.219 (19.354)	-1.789	0.075	50.095 (20.420)	52.475 (18.722)	-1.641	0.103
	HRV_MinNN	816.058 (85.715)	799.509 (91.344)	3.416	0.001	795.171 (78.586)	783.908 (85.448)	2.061	0.040	768.469 (75.479)	764.263 (78.021)	0.806	0.421	752.027 (82.696)	745.047 (79.110)	0.929	0.354
	HRV_MaxNN	853.101 (88.191)	844.560 (77.854)	2.376	0.018	871.713 (87.160)	864.116 (74.724)	1.943	0.053	896.330 (92.453)	892.608 (81.440)	0.837	0.404	905.007 (96.092)	905.597 (84.897)	-0.112	0.911
	HRV_HTI	2.076 (0.505)	2.117 (0.615)	-0.918	0.359	3.367 (1.083)	3.311 (1.202)	0.562	0.575	4.994 (1.757)	4.883 (1.537)	0.694	0.488	6.076 (2.033)	6.031 (1.685)	0.209	0.835
	HRV_TINN	0.000 (0.000)	0.000 (0.000)	-1.501	0.030	10.209 (31.146)	10.894 (39.131)	-0.230	0.818	41.455 (49.042)	51.398 (62.732)	-1.915	0.057	63.968 (66.125)	66.170 (72.248)	-0.282	0.778
	PPG_Rate_Mean	-	-	-	-	-	-	-	-	72.166 (7.225)	72.364 (7.406)	-0.467	0.641	-0.656 (4.154)	-0.445 (4.153)	-2.013	0.048
	RSP_Mean	0.238 (3.824)	0.081 (3.782)	1.396	0.164	0.214 (3.838)	0.027 (3.787)	1.587	0.114	0.398 (3.635)	0.249 (3.704)	1.812	0.072	1.663 (1.282)	1.801 (1.370)	-1.542	0.128
	RSP	RSP_Std_dev	1.438 (1.323)	1.549 (1.382)	-1.976	0.049	1.505 (1.396)	1.690 (1.489)	-2.728	0.007	1.582 (1.377)	1.729 (1.489)	-2.720	0.007	-0.654 (4.213)	-0.279 (4.093)	-2.904
RSP_Median		0.224 (3.961)	0.098 (3.949)	0.928	0.354	0.198 (3.989)	0.088 (3.904)	0.783	0.435	-0.866 (4.373)	-0.614 (4.313)	-2.231	0.028	1.999 (4.018)	2.248 (3.979)	-3.052	0.003
RSP_Max_value		2.364 (3.151)	2.418 (2.882)	-0.543	0.587	2.511 (3.114)	2.605 (2.841)	-0.974	0.331	1.577 (4.360)	1.721 (4.368)	-3.251	0.002	2.979 (2.549)	2.903 (2.769)	0.874	0.383
RSP_Min_value		-2.004 (5.069)	-2.278 (5.132)	2.084	0.038	-2.259 (5.237)	-2.657 (5.349)	2.627	0.009	-2.534 (5.251)	-2.915 (5.464)	2.306	0.022	-3.123 (5.286)	-3.344 (5.516)	1.073	0.285
RSP_Skewness		0.118 (0.660)	0.189 (0.730)	-1.634	0.103	0.121 (0.746)	0.169 (0.763)	-0.746	0.457	0.043 (0.941)	0.010 (1.035)	0.394	0.694	-0.066 (1.037)	-0.034 (0.976)	-1.037	0.708
RSP_Kurtosis		-0.893 (1.228)	-0.788 (1.814)	-0.934	0.351	-0.672 (1.890)	-0.669 (1.775)	-0.020	0.984	-0.175 (3.098)	-0.033 (3.865)	-0.477	0.634	0.118 (3.364)	-0.009 (3.122)	0.461	0.646
EDA_Mean		6.312 (4.961)	6.346 (5.224)	-2.217	0.029	6.618 (5.243)	6.410 (5.233)	0.467	0.641	6.715 (5.513)	6.426 (5.473)	4.303	0.000	6.699 (5.391)	6.246 (5.293)	3.854	0.000
EDA_Std		0.002 (0.003)	0.002 (0.006)	-0.119	0.905	0.011 (0.019)	0.012 (0.031)	-0.835	0.405	0.095 (0.127)	0.091 (0.265)	0.171	0.864	0.197 (0.151)	0.182 (0.448)	0.402	0.688
EDA_Max		6.315 (4.962)	6.349 (5.225)	-0.119	0.905	6.637 (5.248)	6.430 (5.236)	0.466	0.642	6.880 (5.567)	6.568 (5.550)	3.694	0.000	7.051 (5.490)	6.519 (5.466)	3.479	0.001
EDA_Min		6.310 (4.961)	6.343 (5.224)	-0.076	0.939	6.603 (5.234)	6.390 (5.232)	0.479	0.633	6.586 (5.465)	6.284 (5.404)	6.036	0.000	6.458 (5.342)	5.966 (5.106)	8.653	0.000
SKT	EDA_Range	0.006 (0.010)	0.006 (0.019)	-0.553	0.581	0.034 (0.061)	0.040 (0.100)	-0.780	0.436	0.295 (0.402)	0.284 (0.820)	0.179	0.858	0.592 (0.454)	0.553 (1.388)	0.329	0.743
	EDA_Num_peaks	2.496 (1.485)	2.619 (1.512)	-0.965	0.335	3.624 (2.782)	4.392 (2.709)	-2.713	0.008	6.245 (5.026)	7.184 (6.137)	-1.392	0.167	7.313 (6.318)	6.597 (6.760)	0.759	0.450
	EDA_Mean_amplitude	0.044 (0.102)	0.025 (0.082)	2.361	0.019	0.070 (0.170)	0.055 (0.149)	0.861	0.391	0.101 (0.261)	0.093 (0.224)	0.324	0.747	0.110 (0.252)	0.099 (0.165)	0.487	0.628
	SKT_Mean	30.933 (1.096)	30.933 (1.096)	1.065	0.288	30.911 (1.090)	30.910 (1.089)	0.793	0.428	30.917 (1.081)	30.915 (1.108)	1.233	0.219	30.908 (1.095)	30.906 (1.095)	1.003	0.318
	SKT_Std	0.002 (0.003)	0.002 (0.002)	1.499	0.135	0.003 (0.004)	0.003 (0.004)	1.498	0.136	0.005 (0.005)	0.004 (0.005)	1.469	0.143	0.007 (0.007)	0.006 (0.007)	2.200	0.029
	SKT_Max	30.939 (1.094)	30.937 (1.094)	1.751	0.081	30.918 (1.088)	30.916 (1.087)	1.535	0.126	30.926 (1.104)	30.924 (1.104)	2.018	0.045	30.921 (1.088)	30.917 (1.090)	1.919	0.057
	SKT_Min	30.928 (1.097)	30.928 (1.097)	0.366	0.715	30.904 (1.091)	30.904 (1.091)	0.019	0.985	30.907 (1.112)	30.907 (1.112)	0.273	0.785	30.895 (1.102)	30.895 (1.102)	0.367	0.714
	SKT_Range	0.010 (0.009)	0.009 (0.008)	1.423	0.156	0.014 (0.012)	0.012 (0.011)	1.469	0.143	0.019 (0.017)	0.017 (0.016)	1.801	0.073	0.026 (0.023)	0.023 (0.023)	1.521	0.131
	SKT_Slope	-0.000 (0.000)	-0.000 (0.000)	-1.815	0.071	-0.000 (0.000)	0.000 (0.000)	-2.629	0.009	-0.000 (0.000)	-0.000 (0.000)	1.000	0.319	-0.000 (0.000)	-0.000 (0.000)	-0.332	0.740

¹ The symbol '-' indicates that certain metrics are typically computed over longer time windows and cannot be calculated within the short epoch duration.

² The p-values highlighted with gray shading in the table denote statistical significance at the level of $p < 0.05$.

Table 4

Comparative performance of baseline MER methods on the MMME dataset for three-class and seven-class classification

Methods		Three-Class				Seven-Class			
		Acc (%)	F1	UF1	UAR	Acc (%)	F1	UF1	UAR
Hand-Crafted MER	LBP-TOP (2007) [83]	40.79	0.3957	0.3303	0.3443	26.56	0.2272	0.1866	0.1741
	MDMO (2015) [38]	44.22	0.4534	0.4416	0.3228	29.94	0.2634	0.2524	0.2623
	Bi-WOOF (2018) [84]	50.26	0.4823	0.4111	0.4094	34.52	0.3309	0.2805	0.2722
Deep Learning MER	RCN-A (2020) [85]	65.35	0.6234	0.5635	0.5424	38.78	0.3502	0.2981	0.2526
	MERSiamC3D (2021) [86]	70.89	0.6827	0.6625	0.6344	40.43	0.4101	0.3092	0.3246
	FeatRef (2022) [87]	72.46	0.7080	0.6339	0.6075	43.34	0.4234	0.3543	0.3303
	MoExt (2024) [88]	<u>74.23</u>	0.7254	0.6824	0.7035	<u>46.27</u>	<u>0.4541</u>	0.3782	0.3475
	HTNet (2024) [89]	74.96	<u>0.7326</u>	0.7072	0.7171	47.64	0.4543	<u>0.3766</u>	0.3550
	CSARNet (2025) [90]	74.05	0.7576	<u>0.6958</u>	<u>0.7042</u>	44.55	0.4434	0.3582	<u>0.3529</u>

¹ Three-class classification includes negative, positive, and neutral emotions; seven-class classification comprises happiness, sadness, surprise, fear, anger, disgust, and contempt.

² The best results are highlighted in bold, and the second best are underlined.

Table 5

Comparative performance of baseline MER methods across five datasets for three-class classification

Methods	SMIC		CASME II		SAMM		CAS(ME) ³		MMME	
	UF1	UAR	UF1	UAR	UF1	UAR	UF1	UAR	UF1	UAR
RCN-A (2020) [85]	0.6326	0.6441	0.8512	0.8123	0.7601	0.6715	0.3928	0.3893	0.5635	0.5424
MERSiamC3D (2021) [86]	0.7356	0.7598	0.8818	0.8763	0.7475	0.7280	-	-	0.6625	0.6344
FeatRef (2022) [87]	0.7011	0.7083	0.8915	0.8873	0.7372	0.7155	0.3493	0.3413	0.6339	0.6075
MoExt (2024) [88]	0.7976	0.7803	0.8992	0.8912	0.8135	0.8100	0.5457	0.5784	0.6824	0.7035
HTNet (2024) [89]	0.8049	0.7905	0.9101	0.9119	0.8131	0.8124	0.5767	0.5415	0.7072	0.7171
CSARNet (2025) [90]	0.7605	0.7639	0.9254	0.9298	0.7894	0.7924	-	-	0.6958	0.7042

¹ The '-' in the table indicates that the information is not provided in the original paper.

4.2.1. MER based on Visual Information

Data Preprocessing. To effectively reduce the interference of non-facial regions in ME frame sequences during feature analysis, all ME videos were preprocessed prior to the recognition experiments, as illustrated in Fig. 8(a). First, leveraging the distinct separability between facial skin tones and the green background in the HSV color space, precise segmentation of the facial region was achieved. Subsequently, a face detection algorithm² provided by Alibaba Cloud was employed to identify and crop the facial area in the initial frame. This region was then consistently applied to crop the same area across all subsequent frames in the sequence. This approach is based on the observation that MEs are brief, subtle facial movements with minimal positional changes between consecutive frames, whereas frame-by-frame face detection may introduce inconsistencies and disrupt the temporal continuity of MEs. Finally, all cropped facial regions were resized to a uniform resolution of 128×128 pixels to ensure consistency in feature extraction and to enhance computational efficiency.

MER performance. In this section, we adopted two categories of benchmark methods: handcrafted feature-based approaches and deep learning-based approaches. The handcrafted methods include LBP-TOP [91], MDMO [92], and Bi-WOOF [84]. LBP-TOP extends local binary patterns to three dimensions by integrating texture features from X-Y,

X-T, and Y-T planes. MDMO employs optical flow across 36 facial regions of interest to detect micro-movements, while Bi-WOOF uses dual-weighted optical flow and strain magnitudes to enhance apex frame discrimination. The evaluated deep learning methods comprise RCN-A [85], MERSiamC3D [86], FeatRef [87], MoExt [88], HTNet [89], and CSARNet [90]. RCN-A adapts a recurrent convolutional network with three parameter-free modules to improve representation across multiple perspectives, maintaining a shallow architecture suitable for lower-resolution data. MERSiamC3D introduces a two-stage learning framework, involving prior and target learning, based on a Siamese 3D convolutional neural network for MER. FeatRef proposes a feature refinement approach with an expression proposal module incorporating an attention mechanism and a classification branch. MoExt develops a motion extraction strategy, pre-training the feature separator and motion extractor with contrastive loss to capture representative motion features. HTNet leverages hierarchical transformers to identify key facial movement regions through local temporal and global semantic representations. CSARNet implements a local feature augmentation strategy to enhance the local feature representations of motion flow images. Additionally, it incorporates a lightweight backbone network designed to reduce model complexity and computational time while accurately extracting discriminative ME information across channel and spatial dimensions, thereby facilitating effective emotion

²<https://vision.aliyun.com/facebody>

recognition. For fairness, all hyperparameters—including feature map size, batch size, and learning rate—are kept consistent with the default configurations reported in the original papers. During the evaluation, we adopted several commonly used metrics from the MER task in MEGC2019 [93], including Accuracy (Acc), F1-score, Unweighted F1 Score (UF1), and Unweighted Average Recall (UAR), along with Leave-One-Subject-Out Cross-Validation (LOSO-CV) protocol.

Table 4 presents the comparative performance of baseline MER methods on the MMME dataset for three-class and seven-class classification, demonstrating that the samples in the MMME dataset exhibit good separability and discriminative capability. For instance, the Bi-WOOF model achieved an accuracy of 50.26% in the three-class classification task and 34.52% in the seven-class task, while the HTNet model attained 74.96% and 47.64% accuracy, respectively. The deep learning methods outperformed traditional handcrafted feature-based approaches, owing to their superior ability to extract discriminative spatiotemporal features and model subtle facial movement patterns through nonlinear representations. Among these deep learning models, HTNet achieves the highest performance, owing to its hierarchical architecture that facilitates multi-scale feature extraction, significantly improving the accuracy of MER. Then, we conducted comprehensive comparisons of these deep learning methods on five benchmark ME datasets (SAMM, CASME II, SMIC, CAS(ME)³, and our proposed MMME) for three-class classification, as detailed in Table 5. The experimental results demonstrate that these models achieved competitive recognition performance on the MMME dataset, with UF1 and UAR metrics generally outperforming those on the CAS(ME)³ dataset.

4.2.2. MER based on Multimodal Fusion

Recent studies have increasingly highlighted the importance of incorporating multimodal data in ME analysis, with the dual objectives of leveraging more comprehensive emotional representations and overcoming the limitations of unimodal approaches. In this section, we proposed a multimodal fusion-based MER framework to validate the effectiveness of the MMME dataset in multimodal research. The pipeline is outlined as follows:

Data Preprocessing. For MEs, the key frames were processed following the data preprocessing procedure described in Section 4.2.1. The EEG signal was first passed through a filter bank, decomposing it into five frequency bands: 0.5–4 Hz (δ), 4–8 Hz (θ), 8–14 Hz (α), 14–30 Hz (β), and 30–47 Hz (γ). Subsequent preprocessing involved down-sampling to reduce data complexity, followed by independent component analysis (ICA) to isolate distinct signal components. The Adjust algorithm was then applied to remove artifacts and noise. The resulting output yielded cleaned waveforms corresponding to the β , α , θ , δ , and γ bands, facilitating further analysis of brain activity patterns. The PERI-PS analyzed in this section include PPG, ECG, RSP, SKT, and EDA. Initially recorded at a sampling rate of 1000 Hz, these signals

were downsampled to 200 Hz to reduce processing time. Low-frequency drifts over time were removed to eliminate trends in the signals. To reduce noise, Butterworth low-pass filters with different cutoff frequencies were applied based on the characteristics of each signal. For the ECG signal, a Butterworth low-pass filter with a cutoff frequency of 40 Hz was used to remove high-frequency noise. As the EDA signal reflects slow changes in skin conductance, a lower cutoff frequency of 5 Hz was applied to retain these slow changes while eliminating faster fluctuations or noise. For RSP, a low-pass cutoff frequency of 1 Hz was used in the Butterworth filter.

Feature Extraction. To effectively capture the motion characteristics of MEs, this study utilized the FlowNet 2.0 algorithm³ to extract optical flow features, focusing on subtle movements in MEs. A schematic diagram of this process is depicted in Fig. 8(a). The optical flow feature map is formulated as follows:

$$V = (u(x, y), v(x, y)) \mid x = 1, 2, \dots, X, y = 1, 2, \dots, Y, \quad (4)$$

where X and Y represent the width (W) and height (H) of the image, respectively, and $u(x, y)$ and $v(x, y)$ denote the horizontal and vertical component of optical flow feature map V ($V = [V_x, V_y]$), with $V \in \mathbb{R}^{W \times H \times 2}$. Additionally, the optical strain provides insights into the degree of facial displacement, thereby offering valuable information about the subtle movements during MEs. The optical strain is derived from the gradient of the optical flow field and is expressed as:

$$V_z = \sqrt{\frac{\partial V_x^2}{\partial x} + \frac{\partial V_y^2}{\partial y} + \frac{1}{2} \left(\frac{\partial V_x^2}{\partial y} + \frac{\partial V_y^2}{\partial x} \right)}, \quad (5)$$

where $\frac{\partial V_x^2}{\partial x}$, $\frac{\partial V_y^2}{\partial y}$, $\frac{\partial V_x^2}{\partial y}$ and $\frac{\partial V_y^2}{\partial x}$ are the partial first-order derivatives of V . Finally, three-dimension optical flow feature maps are represented as $V_m = [V_x, V_y, V_z]$, with $V_m \in \mathbb{R}^{W \times H \times 3}$.

Inspired by Saffaryazdi [105], we consider the apex frame as the point of peak emotional intensity in each trial. A fixed-length time window centered on the apex frame is designated as the region of interest (ROI), and only the physiological data within this window are used for analysis. When selecting the ROI window size, we observed that an excessively large window may cause overlap between ROIs of adjacent MEs, while a window that is too small may result in the loss of important features. Based on these observations, we set the window size to 10 s. Based on the concordance analysis between MEs and PERI-PS in Section 4.1, relevant literatures, and medical expert knowledge, this study extracted a series of PERI-PS features significantly associated with emotions, as shown in Table 6. PPG was used to assess the mechanical activity of the heart, from

³<https://github.com/NVIDIA/flownet2-pytorch>

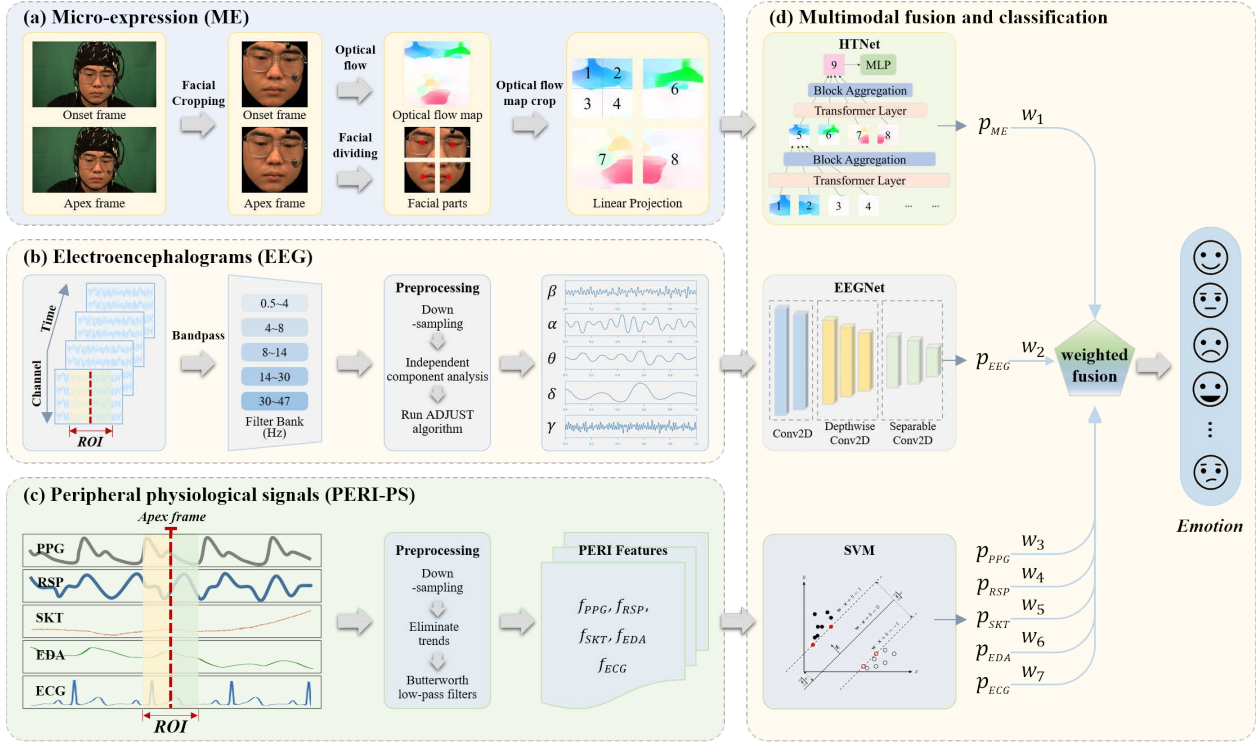


Figure 8: The proposed multimodal MER framework integrating MEs and PS. The framework first performs preprocessing and feature extraction for each modality, followed by decision-level fusion through a weighted voting strategy to combine the outputs of multiple classifiers.

which pulse rate (PR) was derived to reflect variations in cardiac rhythm. ECG, by contrast, recorded the heart's electrical activity. In addition to heart rate (HR), we extracted HRV features, including the standard deviation of successive NN intervals (SDSD), the standard deviation of NN intervals (SDNN), and the root mean square of successive NN interval differences (RMSSD), all of which are closely linked to emotional fluctuations. RSP patterns were obtained by detecting the extrema of breathing cycles, with features such as amplitude differences, mean, and standard deviation of the respiration rate. For SKT, we extracted statistical features including the mean, standard deviation, maximum, and minimum values. EDA reflects sympathetic nervous system arousal, typically indicated by marked changes during emotional stress. We analyzed both the skin conductance level (SCL), representing slower changes, and the skin conductance response (SCR), reflecting rapid fluctuations. Finally, all signals underwent normalization. The preprocessing and feature extraction procedures for the PS were implemented using NeuroKit2⁴, an open-source neurophysiological processing toolbox. The resulting emotion-related features can be mathematically defined as follows:

$$f_{PERI-PS} = [f_{PPG}, f_{ECG}, f_{RSP}, f_{SKT}, f_{EDA}]. \quad (6)$$

Multimodal Fusion and Classification. To improve MER performance, we implement a multi-classifier voting

framework that capitalizes on the complementary discriminative capabilities of diverse classifiers. The system integrates seven modality-specific sub-classifiers: the ME classifier utilizes HTNet [89], the EEG classifier employs EEGNet [106], and the five PERI-PS classifiers utilize SVMs. HTNet includes two major components: a transformer layer that leverages the local temporal features and an aggregation layer that extracts local and global semantical facial features, achieving optimal performance on the MMME dataset, as shown in Table 4. EEGNet is chosen due to its compact, efficient convolutional neural network architecture, tailored for processing complex EEG signal. SVMs are adopted for PERI-PS classification due to the lower-dimensional and less complex nature of these signals compared to ME or EEG data, as SVMs excel at identifying optimal decision boundaries for PS features. Following individual emotion classification by each sub-classifier, a weighted voting scheme synthesizes the final prediction. A novel feedback-driven weighting mechanism was developed to optimize decision fusion. This approach dynamically adjusts voting weights by incorporating both the inherent reliability of each modality, and the real-time classification accuracy of PS-based emotion recognition. The methodological details of this adaptive weighting strategy are illustrated in Fig. 8(c), comprising the following key steps:

Step 1: Calculate the weighted matrix W_i for each sub-classifier based on the classification accuracy of its respective modality. Each sub-classifier, corresponding to a single

⁴<https://neuropsychology.github.io/NeuroKit/index.html>

Table 6

List of extracted expert-defined and statistical features from the recorded PERI-PS

Modality	Features	Description	Reference
PPG	<i>PR</i>	Pulse rate	[94]
	<i>HR</i>	Mean heart rate	[95]
	<i>SDSD</i>	Standard deviation of successive NN intervals	[96, 97]
	<i>SDNN</i>	Standard deviation of NN intervals	[96, 97]
ECG	<i>RMSDD</i>	Root mean square of successive differences	[96, 97]
	<i>LF, HF</i>	Low and high-frequency component in the range of 0.05-0.15 Hz and 0.15-0.4 Hz of the Welch spectrum	[96, 97]
	<i>LF_n, HF_n</i>	Normalized HF and LF spectrum	[96, 97]
	<i>LF/HF</i>	Ratio of the LF and HF component	[96, 97]
	<i>SD1/SD2</i>	Ratio of SD1 and SD2 as standard deviation along the identity lines of a Poincaré plot	[96, 97]
	<i>PSS</i>	Percentage of short segments	[98, 99]
	<i>PIP</i>	Percentage of inflection points in NN intervals	[98, 99]
RSP	<i>μ_{BR}, σ_{BR}</i>	Mean and standard deviation of breathing rate	[100]
	<i>μ_[E-I]</i>	Mean of the ratio of inhalation and exhalation amplitude values	[100]
SKT	<i>μ_T, σ_T</i>	Mean and standard deviation of the skin temperature	[101, 102]
	<i>min_T, max_T</i>	Minimal and maximal of the temperature	[101, 102]
EDA	$\sum_i^W SCL'(t)$	Change of the skin conductance level	[62, 103, 104]
	$\frac{\#Peaks}{SCR}/W$	Number of peaks as measure of the phasic component	[62, 103, 104]
	$\mu_{SCR}^{Amplitude}$	Mean amplitude values of SCR peaks	[62, 103, 104]
	μ_{SCR}^{Rise}	Mean rise time of SCR peaks	[62, 103, 104]
	$\mu_{SCR}^{Recovery}$	Mean recovery time to 50 percent of the maximal peak amplitude	[62, 103, 104]

modality, is independently trained and tested to determine the recognition accuracy for each emotional state:

$$\vec{P}_i = (p_{i1}, \dots, p_{ij})^T, i \in \{1, 2, \dots, 7\}, \quad (7)$$

where $p_{ij} \in [0, 1]$ represents the predicted probability of the j -th emotional state by the i -th sub-classifier, and $j \in \{1, 2, \dots, m\}$. Using a feedback-based principle, the weighted matrix for each modality is determined as follows:

$$W_i = \begin{bmatrix} p_{i1} & \dots & 0 \\ \vdots & \ddots & \vdots \\ 0 & \dots & p_{ij} \end{bmatrix}, i \in \{1, 2, \dots, 7\}, \quad (8)$$

where W_i is the weighted matrix of the i -th modality.

Step 2: Let $\vec{C}_i = (c_{i1}, \dots, c_{ij})^T$ ($1 \leq i \leq 7$) represent the recognition result of each sub-classifier, where $|\vec{C}_i| = 1$ and $c_{ij} \in \{0, 1\}$. The weighted matrices and recognition results of each sub-classifier are then linearly fused as follows:

$$\vec{C} = \sum_{i=1}^7 W_i \vec{C}_i = \sum_{i=1}^7 \begin{bmatrix} p_{i1} & \dots & 0 \\ \vdots & \ddots & \vdots \\ 0 & \dots & p_{ij} \end{bmatrix} \begin{bmatrix} c_{i1} \\ \vdots \\ c_{ij} \end{bmatrix} = \begin{bmatrix} \sum_{i=1}^7 c_{i1} p_{i1} \\ \vdots \\ \sum_{i=1}^7 c_{ij} p_{ij} \end{bmatrix}. \quad (9)$$

Step 3: Based on the maximum score rule, the emotional state with the highest score, denoted as class k is selected as the final recognition result:

$$MAX_{j=1}^m \left\{ \sum_{i=1}^7 c_{ij} p_{ij} \right\} = \sum_{i=1}^7 c_{ik} p_{ik}. \quad (10)$$

Through this approach, this study effectively integrated the recognition results from multiple sub-classifiers, thereby enhancing the reliability of the final classification.

Fig. 9 presents a comparative evaluation of the recognition accuracy for seven basic emotions across various modalities, encompassing unimodal methods (ME, EEG, and PERI) and a multimodal fusion approach (ME+EEG+PERI). The experimental findings reveal that ME generally achieve superior classification accuracy for the majority of emotions, surpassing unimodal methods reliant on EEG or PERI. For instance, ME achieve the highest recognition rates for fear (57.74%±3.46), disgust (56.81%±3.78), and happiness (48.45%±3.34), potentially due to the more pronounced facial muscle movement features associated with these emotions, which offer greater discriminability compared to PS. However, for certain emotions such as surprise and contempt, the ME based method is less effective than EEG, possibly due to the MEs for these emotions are subtler and harder to capture accurately through facial movements. Although PERI exhibit a relatively lower overall recognition rate, they provide supplementary value in identifying disgust (40.57%±5.67), highlighting the unique complementary strengths of different modal signals in emotion recognition. By integrating the complementary information from ME, EEG, and PERI, the multimodal fusion method (ME+EEG+PERI) significantly enhances overall emotion recognition performance. For instance, the recognition accuracy for happiness increases from 48.45% in the ME modality to 52.24% in the fusion model, for surprise from 39.73% to 46.83%, and for sadness from 43.09% to 47.77%. These findings substantiate the synergistic effect of visual and PS within the MMME dataset. Additionally, Tables 7 and 8 provide detailed performance metrics, including

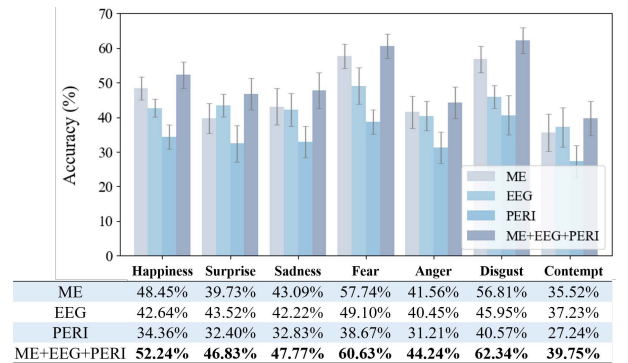


Figure 9: A comparative analysis of seven basic emotion recognition accuracies across different modalities, highlighting the superiority of multimodal fusion.

Table 7

Seven-class emotion classification performance across different modality combinations

Modality Type	Acc(%) (mean±std)	F1 (mean±std)	UF1 (mean±std)	UAR (mean±std)
ME	47.64±3.18	0.4543±0.0245	0.3766±0.0333	0.3550±0.0278
EEG	42.19±2.47	0.4089±0.0311	0.3447±0.0256	0.3312±0.0305
PERI	33.45±3.23	0.3256±0.0322	0.2998±0.0277	0.2776±0.0286
ME+EEG+PERI	49.38±3.22	0.4894±0.0473	0.4021±0.0384	0.3887±0.0423

¹ Bold font indicates the best-performing results.

Table 8

Three-class emotion classification performance across different modality combinations

Modality Type	Acc(%) (mean±std)	F1 (mean±std)	UF1 (mean±std)	UAR (mean±std)
ME	74.96±4.78	0.7326±0.0636	0.7072±0.0439	0.7171±0.0588
EEG	69.12±5.66	0.6628±0.0572	0.5834±0.0480	0.5522±0.0452
PERI	52.45±3.29	0.5034±0.0452	0.4205±0.0438	0.4137±0.0578
ME+EEG+PERI	77.46±5.66	0.7525±0.0470	0.7343±0.0673	0.7455±0.0479

¹ Bold font indicates the best-performing results.

Acc (%), F1 score, UF1, and UAR, for different modalities across three-class and seven-class emotion recognition tasks, demonstrating that the fused modality consistently outperforms individual modalities. This further underscores the significant advantages of the multimodal fusion strategy in enhancing emotion recognition efficacy.

The confusion matrix in Fig. 10 clearly illustrates the relationship between the model’s predicted results and the true labels, offering a detailed analysis of the model’s classification performance. The diagonal elements of the matrix represent the proportion of correctly classified samples, with darker colors indicating higher accuracy. It can be observed that in the three-class task, the classification performance based on ME outperforms EEG, while PERI yields the lowest accuracy. The multimodal fusion approach performs best, with a significantly reduced misclassification rate and a relatively balanced accuracy distribution across classes. In contrast, the seven-class task exhibits a pronounced class imbalance issue. The confusion matrix reveals that the classification accuracy for “Fear,” “Disgust,” and “Surprise” is relatively high, likely due to these emotions being easier to elicit, with more distinct facial expressions and physiological responses. Conversely, the accuracy for “Anger” and “Contempt” is lower, possibly because these MEs are harder to induce, resulting in fewer samples and consequently poorer model performance on these classes. The multimodal fusion method demonstrates significant advantages in emotion recognition, particularly in fine-grained seven-class tasks, effectively improving classification accuracy. However, certain emotions (e.g., “Anger” and “Contempt”) still exhibit high misclassification rates, suggesting that improvements to the MMME dataset should focus on increasing sample size and enhancing class balance.

Visual Analysis. To gain deeper insights into the learned features of MEs, we utilize Grad-CAM to visualize activation heatmaps, as shown in Fig. 11. This visualization analysis demonstrates the HTNet model’s ability to focus on different regions and visual features in facial images.

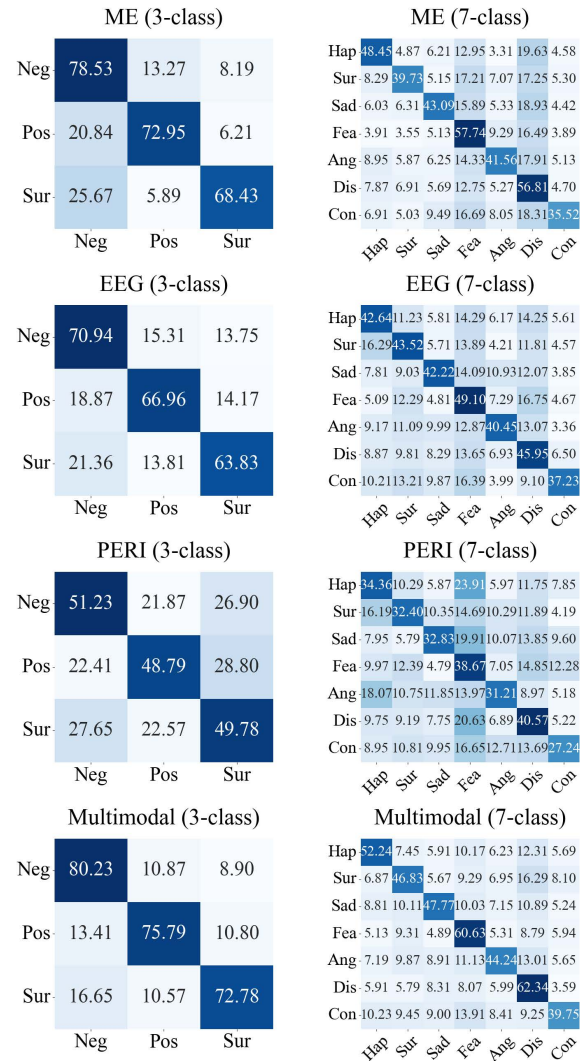


Figure 10: Confusion matrices for emotion classification (three-class and seven-class) across various modalities.

A sample from each of the seven emotional categories is selected, and Grad-CAM is applied to the output of the model’s final convolutional layer. The generated heatmap is then overlaid on the original sample image. The highlighted regions correspond to areas crucial for recognizing subtle MEs, such as the eyebrows and corners of the mouth. For instance, in the “Happiness” sample, the Grad-CAM heatmap highlights the zygomaticus major muscle, corresponding to AU12, with the action descriptor “Lip corner puller.” In the “Surprise” sample, the highlighted regions include the frontalis (pars lateralis) and masseter muscles, corresponding to AU2 (“Outer brow raiser”) and AU26 (“Jaw drop”), respectively. In the “Sadness” sample, the highlighted region corresponds to the frontalis (pars medialis), associated with AU1 (“Inner brow raiser”). For the “Contempt” sample, the zygomaticus major muscle is highlighted, corresponding to AU12 (“Lip corner puller”). These results indicate that the visual feature learning model employed in this study is capable of focusing on key visual regions that are closely

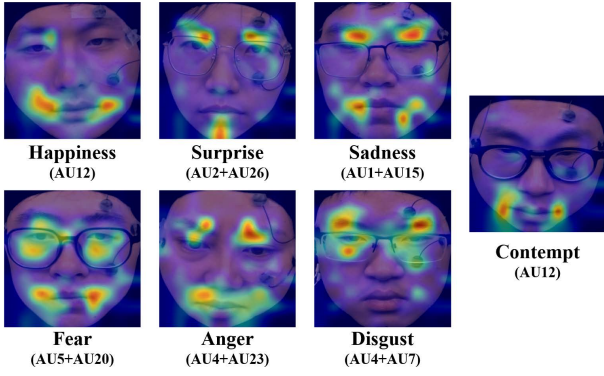


Figure 11: Visual Explanations of ME via Gradient-Based Localization.

related to the target task during the decision-making process. This finding further highlights the pivotal role of visual features in multimodal fusion.

4.3. ME Spotting Validation

To further validate the effectiveness and practical value of the proposed MMME dataset, this section investigates ME spotting tasks based on the dataset, encompassing both unimodal (visual-only) and multimodal (visual-ECG fusion) approaches. This serves as a preliminary exploration toward advancing ME spotting from unimodal to multimodal frameworks. Fig. 12 illustrates the ME spotting pipeline, which incorporates a Candidate Clip Filter (CCF) module to improve the detection results.

4.3.1. ME Spotting based on Visual Information

ME spotting aims to locate the onset, apex, and offset frames of MEs within continuous video streams, and holds significant potential for real-world applications. Considering the characteristics of the dataset, we design two types of detection tasks: a unimodal ME spotting task based solely on video, and a multimodal ME spotting task that incorporates auxiliary ECG signals. These tasks not only facilitate the evaluation of the dataset's quality in terms of spatiotemporal annotations and multimodal synchronization but also enable the exploration of the complementary roles of video and

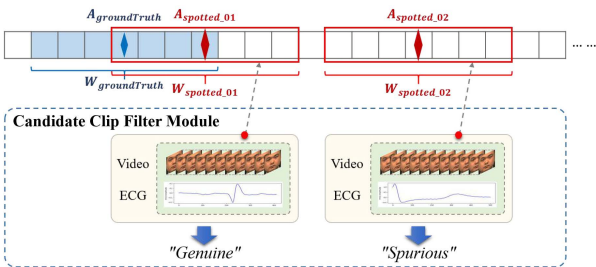


Figure 12: Schematic diagram of the ME spotting pipeline. The blue-filled regions denote the ground-truth ME from manual annotation, while the red-bordered boxes represent the automatically detected results. We propose a Candidate Clip Filter (CCF) module to enhance the accuracy of ME spotting.

PS in ME spotting, thereby laying a new foundation for the advancement of multimodal ME spotting technologies.

Evaluation Metrics. In ME spotting task, Intersection over Union (IoU) serves as a widely adopted evaluation metric that treats ME spotting as an object detection problem. IoU quantifies detection performance by calculating the degree of overlap between the temporal interval of an ME sample and the interval identified by the detection algorithm. Based on the computed IoU value, a detected interval is classified as either a true positive (TP) or a false positive (FP). Specifically, for a detected interval $W_{spotted}$, if there exists a ground-truth ME interval $W_{groundTruth}$ that satisfies the condition defined in Equation 11, the predicted interval is judged as a TP:

$$IoU = \frac{W_{spotted} \cap W_{groundTruth}}{W_{spotted} \cup W_{groundTruth}} \quad (11)$$

$$\text{True Positive: } IoU \geq \epsilon$$

$$\text{False Positive: } IoU < \epsilon$$

following most existing studies, we set the value of ϵ to 0.5.

Experimental Results. Table 9 presents a comparative performance of different ME spotting algorithms across four datasets, which not only evaluates the quality and annotation accuracy of MMME but also establishes performance benchmarks for this task. The algorithms used include MESNet [59], ABPN [107], SL-Swin [108], DMA-LBP [109] and MSOF [110]. MESNet utilizes 2D convolutions to extract spatial features and 1D convolutions to capture temporal dynamics, enabling video clip classification as MEs or non-MEs while regressing their temporal boundaries. ABPN computes frame-level auxiliary probabilities to identify apex or boundary frames, leveraging these probabilities to generate precise expression proposals for localization. SL-Swin employs a Transformer-based approach, integrating Shifted Patch Tokenization and Locality Self-Attention into the Swin Transformer backbone, to predict frame probabilities within expression intervals for effective ME spotting. DMA-LBP applies multiple sliding windows of varying scales and patterns to create weak detectors tailored to MEs of specific durations and transition modes, aggregating their outputs through a voting-based module. MSOF incorporates low-pass filtering and empirical mode decomposition to eliminate high-frequency noise, using non-maximum suppression to delineate final expression intervals for accurate ME spotting. Experimental results demonstrate that the MMME dataset effectively distinguishes the performance of various algorithms. For instance, MSOF achieves a significantly higher F1-score (0.3747) compared to MESNet (0.0511), a level of differentiation consistent with performance on public datasets, confirming the suitability of the MMME dataset for evaluating ME spotting algorithms. Furthermore, the dataset exhibits robust effectiveness in ME spotting, performing comparably to established public datasets such as SAMM, CASME II, and CAS(ME)³. These findings underscore the MMME's

Table 9

Comparative performance of different ME spotting algorithms across four datasets

Method	SAMM			CASME II			CAS(ME) ³			MMME		
	F1-score	Precision	Recall	F1-score	Precision	Recall	F1-score	Precision	Recall	F1-score	Precision	Recall
MESNet (2021) [59]	0.0490	0.0280	0.2300	0.0260	0.0130	0.1800	-	-	-	0.0511	0.0372	0.2963
ABPN (2022) [107]	0.2264	0.2727	0.1935	0.1590	-	-	0.3529	0.3750	0.3333	0.2861	0.3104	0.2547
SL-Swin (2023) [108]	0.0898	0.0689	0.1290	0.0879	0.0556	0.2105	0.1944	0.1944	0.1944	0.2152	0.2290	0.2694
DMA-LBP (2024) [109]	0.0423	0.0230	0.2642	0.0096	0.0048	0.5263	-	-	-	0.1563	0.1350	0.2453
MSOF (2025) [110]	0.3404	0.5000	0.2580	0.3928	0.3854	0.4005	0.3902	0.3478	0.4444	0.3747	0.4356	0.4122

¹ The '-' in the table indicates that the information is not provided in the original paper.

high consistency and discriminative power in algorithm performance evaluation, making it well-suited for testing and validating ME spotting algorithms.

4.3.2. ME Spotting based on Multimodal Fusion

Existing ME spotting algorithms primarily rely on facial visual information. Traditional approaches extract features such as facial landmark displacements, Local Binary Patterns from Three Orthogonal Planes (LBP-TOP), and optical flow vectors. More recent methods leverage deep learning architectures, including CNNs and Transformers, to model the spatiotemporal dynamics of MEs. However, due to the inherently low signal-to-noise ratio of ME signals and the susceptibility of manual annotations to bias, visual-based spotting algorithms often exhibit suboptimal performance and struggle to meet the requirements of real-world applications. Recent studies suggest that physiological responses hold potential value in ME spotting. For instance, Lu *et al.* [111] employed facial EMG to analyze the intensity characteristics of MEs and found that EMG can serve as a distinguishing indicator between micro- and macro-expressions. Similarly, Gupta *et al.* [63] investigated the estimation of instantaneous heart rate from facial videos and demonstrated its utility in enhancing ME spotting performance. Given that human emotional changes are often accompanied not only by MEs but also by fluctuations in heart rate, the co-occurrence of MEs and instantaneous HRV has been widely recognized as a physiological manifestation of emotional arousal. This phenomenon has been extensively applied in lie detection technologies.

In Section 4.1, we analyzed the consistency between MEs and PS. The results reveal a statistically significant correlation ($p < 0.05$) between the occurrence of MEs and certain instantaneous heart rate variability features. This correlation is likely attributable to the fact that both MEs and heart rate responses are jointly regulated by emotional changes and the autonomic nervous system. Specifically, when an individual experiences intense emotional fluctuations, the sympathetic nervous system becomes activated, leading to measurable changes in heart rate. These findings provide a theoretical foundation for this study's approach: investigating the use of ECG features to enhance the accuracy of ME spotting. Fig. 13 illustrates the relationship between ME occurrences and heart rate variability in a representative experimental trial: the upper panel displays the ECG signal waveform, the middle panel shows the temporal trend of heart rate, and the lower panel depicts the variation in heart rate slope. Red vertical lines indicate the precise timestamps of three ME apex frames in this trial, occurring at 12,850 ms, 26,230 ms, and 40,640 ms. Notably, while the absolute heart rate values at these ME events differ, each coincides with a region of elevated heart rate slope (HRS), reflecting instantaneous heart rate changes significantly above the trial's mean. This observation suggests a potential link between ME apex frame and the HRS. To verify the generality of this phenomenon, a statistical analysis was conducted on all ME samples. The results revealed that, among 634 ME samples, 464 ME apex frames corresponded to HRS values exceeding the trial's mean slope ($Mean_{HR_slope}$), representing approximately 73.19%. Additionally, 345 ME apex frames had HRS values surpassing 1.5 times the trial's mean heart rate slope, accounting for approximately 54.41%. These results further confirm a correlation between the occurrence of MEs and significant increases in HRS (i.e., rapid instantaneous changes in heart rate).

Candidate Clip Filter Module. Building upon the aforementioned analysis, we propose a Candidate Clip Filter (CCF) module that integrates HRS features to authenticate detected ME clips: a candidate ME is classified as genuine if the HRS at its apex frame exceeds the trial's mean slope value; conversely, if the slope is less than the mean value, it is classified as a spurious ME. The specific classification rule is detailed in Equation 12:

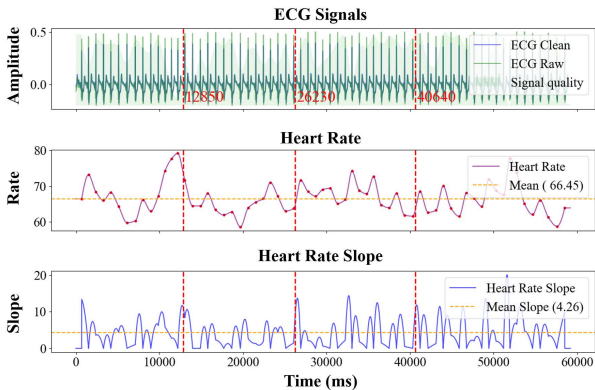


Figure 13: Relationship between MEs and heart rate in a representative experimental trial.

Table 10

Performance of different ME spotting algorithms combined with Candidate Clip Filter (CCF) module on the MMME dataset

Method	F1-score	Precision	Recall
MESNet (2021) [59]	0.0511	0.0372	0.2963
ABPN (2022) [107]	0.2861	0.3104	0.2547
SL-Swin (2023) [108]	0.2152	0.2290	0.2694
DMA-LBP (2024) [109]	0.1563	0.1350	0.2453
MSOF (2025) [110]	0.3747	0.4356	0.4122
MESNet + CCF	0.1067	0.0914	0.2963
ABPN + CCF	0.3646	0.3932	0.2547
SL-Swin + CCF	0.2780	0.2949	0.2694
DMA-LBP + CCF	0.1734	0.1602	0.2453
MSOF + CCF	0.4023	0.4790	0.4122

$$Classify(apex_i) = \begin{cases} Genuine, & \text{if } v_s > Mean_{HR_slope} \\ Spurious, & \text{otherwise} \end{cases}, \quad (12)$$

here, $apex_i$ denotes the apex frame of the i -th candidate ME, v_s represents the slope of the heart rate curve at the apex frame, and $Mean_{HR_slope}$ refers to the average slope of the heart rate curve within the same trial.

Experimental Results. In this section, we evaluate the performance of various ME spotting algorithms on MMME dataset and further analyzes the optimization effects of the CCF module. As shown in Table 10, the original algorithms exhibit varying performance without CCF module, with MSOF achieving significantly higher F1-score (0.3747) and Precision (0.4356) compared to other methods. After integrating CCF, the precision of all algorithms improves (e.g., MSOF + CCF increases to 0.4790), while recall remains unchanged, confirming that CCF enhances prediction reliability by effectively reducing FP. Concurrently, the F1-score shows universal improvement (e.g., SL-Swin + CCF rises from 0.2152 to 0.2780), demonstrating CCF module’s efficacy in balancing precision and recall. The experimental results indicate that the CCF module is effective in enhancing the detection performance of moderately performing algorithms (e.g., ABPN, SL-Swin) while maintaining the superiority of high-performance algorithms (e.g., MSOF), thereby providing an efficient post-processing optimization solution for ME spotting. The findings of this section validate the effectiveness of the PS-assisted ME spotting algorithm, demonstrating the substantial potential of integrating visual information with ECG in ME spotting tasks.

5. Ethical Issues

The research purpose and procedure were explained to each participant before the recording started, and the participants were well-aware that they can stop and quit the recording at anytime. One consent form was signed when the participant understood the contents and agreed to participate. Special questions were asked in the consent

form concerning the data sharing issue, and the participants choose between two levels: 1) all recorded data could be shared and used for research analysis, and facial images and videos can be published or presented for academic purposes, e.g., in paper publications, presentations, webpages, or demos; 2) all recorded data could be shared and used for research analysis, but facial images and videos cannot be published or presented. 62 participants agreed on level-1, and the rest 13 participants agreed on level-2.

6. Conclusion and Perspective

6.1. Conclusion

This study addresses the limitations of micro-expression (ME) research, which has traditionally focused on a single visual modality while neglecting emotional information from other modalities. To overcome this, we developed the Multimodal ME Dataset (MMME), the most comprehensive and rigorously synchronized multimodal dataset to date. For the first time, this dataset enables the simultaneous collection of facial action signals (MEs), central nervous signals (EEG), and peripheral physiological signals (PS)—including PPG, RSP, SKT, EDA and ECG—thereby surpassing the constraints of existing ME corpora. The Continuous Monitoring and Real-Time Reminding (CMRR) paradigm proposed in this study aligns with the core characteristic of MEs as “emotional leakage under controlled conditions.” By minimizing interference, this paradigm achieves a balance between experimental control and ecological validity, significantly enhancing the efficiency of ME elicitation. The MMME dataset, meticulously annotated by multiple experts, comprises 634 MEs, 2,841 macro-expressions (MaEs), and 2,890 trials of multimodal PS. This high-quality dataset provides a robust foundation for exploring the neural mechanisms of MEs and conducting multimodal PS fusion analyses. Concordance analysis between MEs and PS reveals significant correlations between MEs and physiological features such as HRV, RSP, and EDA activity. These findings validate the existence of visual-physiological synergistic effects and offer a theoretical basis for multimodal fusion strategies. Extensive experiments confirm the effectiveness of the MMME dataset: in ME recognition tasks, the proposed multimodal fusion strategies leverage complementary information from different modalities, significantly improving recognition performance. In ME spotting tasks, integrating visual features with heart rate slope effectively eliminates spurious-ME segments, further enhancing detection accuracy. These outcomes advance ME research from single-modality visual analysis to a multimodal fusion paradigm, offering critical support for applications in intelligent human-computer interaction and mental health monitoring.

6.2. Perspective

At the data level, future work will focus on enriching the diversity of the dataset by incorporating participants from various ethnicities, cultural backgrounds, and age groups to

enhance its generalizability and representativeness. Additionally, immersive interactive scenarios will be designed to construct datasets that are more reflective of real-world contexts. At the technical level, efforts will be directed toward advancing multimodal fusion algorithms from “modality stacking” to “mechanism modeling.” This will involve techniques such as semantic alignment of heterogeneous modal data, cross-modal attention mechanisms, and multimodal graph modeling to achieve temporal synchronization and semantic coordination across modalities, thereby advancing multimodal affective computing toward mechanism understanding and reasoning capabilities. At the theoretical level, the application of the “multi-channel emotional expression theory” and the “emotional consistency theory” in the field of MEs will be further deepened. This will include exploring the neural mechanisms of MEs and uncovering the underlying principles of visual-physiological synergistic effects.

Acknowledgments

This work was supported in part by the grants from the National Natural Science Foundation of China under Grant (No.62332019, No.62076250, No.62406338 and No.62204204), the National Key Research and Development Program of China (No.2023YFF1203900 and No.2023YFF1203903), the Innovation Capability Support Program of Shaanxi (2024RS-CXTD-7), the Natural Science Basic Research Plan in Shaanxi Province of China (2023JC-XJ-07).

CRedit authorship contribution statement

Chuang Ma: Conceptualization of this study, Methodology, Writing - Original draft preparation. **Yu Pei:** Data curation, Formal analysis. **Jianhang Zhang:** Data curation, Investigation. **Shaokai Zhao:** Conceptualization of this study, Methodology. **Bowen Ji:** Methodology, Writing - review & editing. **Liang Xie:** Methodology, Validation. **Ye Yan:** Conceptualization of this study, Methodology. **Erwei Yin:** Writing - review & editing, Validation.

References

- [1] Luiz Pessoa. On the relationship between emotion and cognition. *Nat Rev Neurosci.*, 9(2):148–158, 2008.
- [2] Kaouther Ezzameli and Hela Mahersia. Emotion recognition from unimodal to multimodal analysis: A review. *Inf. Fusion*, 99:101847, 2023.
- [3] Jason B Luoma and Christina Chwyl. Interpersonal mechanisms for the maintenance of self-criticism: expressive suppression, emotion expression, and self-concealment. *Current Psychology*, 41(6):4027–4040, 2022.
- [4] Paul Ekman and Wallace V Friesen. Nonverbal leakage and clues to deception. *Psychiatry*, 32(1):88–106, 1969.
- [5] Yante Li, Jinsheng Wei, Yang Liu, Janne Kauttonen, and Guoying Zhao. Deep learning for micro-expression recognition: A survey. *IEEE Transactions on Affective Computing*, 13(4):2028–2046, 2022.
- [6] William E Rinn. The neuropsychology of facial expression: a review of the neurological and psychological mechanisms for producing facial expressions. *Psychological bulletin*, 95(1):52, 1984.
- [7] Jane Lee and Maria Rosaria Muzio. Neuroanatomy, extrapyramidal system. *StatPearls Publishing, Treasure Island (FL)*, 2020.
- [8] Hong-Xia Xie, Ling Lo, Hong-Han Shuai, and Wen-Huang Cheng. An overview of facial micro-expression analysis: Data, methodology and challenge. *IEEE Trans. Affective Comput.*, 14(3):1857–1875, 2022.
- [9] P Sriram Kumar, Praveen Kumar Govarthan, Abdul Aleem Shaikh Gadda, Nagarajan Ganapathy, and Jac Fredo Agastinose Ronickom. Deep learning-based automated emotion recognition using multi modal physiological signals and time-frequency methods. *IEEE Transactions on Instrumentation and Measurement*, 2024.
- [10] Priyadarsini Samal and Mohammad Farukh Hashmi. Role of machine learning and deep learning techniques in eeg-based bci emotion recognition system: a review. *Artif. Intell. Rev.*, 57(3):50, 2024.
- [11] Essam H Houssein, Asmaa Hammad, and Abdelmegeid A Ali. Human emotion recognition from eeg-based brain-computer interface using machine learning: a comprehensive review. *Neural Comput. Appl.*, 34(15):12527–12557, 2022.
- [12] Dongjun Liu, Weichen Dai, Hangkui Zhang, Xuanyu Jin, Jianting Cao, and Wanzeng Kong. Brain-machine coupled learning method for facial emotion recognition. *IEEE Trans. Pattern Anal. Mach. Intell.*, 45(9):10703–10717, 2023.
- [13] Sihem Nita, Salim Bitam, Matthieu Heidet, and Abdelhamid Melouk. A new data augmentation convolutional neural network for human emotion recognition based on eeg signals. *Biomed. Signal Process. Control*, 75:103580, 2022.
- [14] Luis R Mercado-Diaz, Yedukondala Rao Veeranki, Fernando Marmolejo-Ramos, and Hugo F Posada-Quintero. Eda-graph: Graph signal processing of electrodermal activity for emotional states detection. *IEEE J. Biomed. Health. Inf.*, 2024.
- [15] Yi-Hsuan Chang, Rachel Yep, and Chin-An Wang. Pupil size correlates with heart rate, skin conductance, pulse wave amplitude, and respiration responses during emotional conflict and valence processing. *Psychophysiol.*, page e14726, 2024.
- [16] Stanisław Saganowski, Bartosz Perz, Adam G Polak, and Przemysław Kazienko. Emotion recognition for everyday life using physiological signals from wearables: A systematic literature review. *IEEE Trans. Affective Comput.*, 14(3):1876–1897, 2022.
- [17] Jingting Li, Zizhao Dong, Shaoyuan Lu, Su-Jing Wang, Wen-Jing Yan, Yinhuang Ma, Ye Liu, Changbing Huang, and Xiaolan Fu. Cas (me) 3: A third generation facial spontaneous micro-expression database with depth information and high ecological validity. *IEEE Trans. Pattern Anal. Mach. Intell.*, 45(3):2782–2800, 2022.
- [18] Liangfei Zhang, Xiaopeng Hong, Ognjen Arandjelović, and Guoying Zhao. Short and long range relation based spatio-temporal transformer for micro-expression recognition. *IEEE Trans. Affective Comput.*, 13(4):1973–1985, 2022.
- [19] Sirui Zhao, Huaying Tang, Xinglong Mao, Shifeng Liu, Yiming Zhang, Hao Wang, Tong Xu, and Enhong Chen. Dfme: A new benchmark for dynamic facial micro-expression recognition. *IEEE Trans. Affective Comput.*, 2023.
- [20] Ren Zhang, Ning He, Ying Wu, Yuzhe He, and Kang Yan. To balance: balanced micro-expression recognition. *Multimedia Syst.*, pages 1–11, 2022.
- [21] Tomas Pfister, Xiaobai Li, Guoying Zhao, and Matti Pietikäinen. Recognising spontaneous facial micro-expressions. In *2011 international conference on computer vision*, pages 1449–1456. IEEE, 2011.
- [22] Wen-Jing Yan, Qi Wu, Yong-Jin Liu, Su-Jing Wang, and Xiaolan Fu. Casme database: A dataset of spontaneous micro-expressions collected from neutralized faces. In *2013 10th IEEE international conference and workshops on automatic face and gesture recognition (FG)*, pages 1–7. IEEE, 2013.
- [23] Wen-Jing Yan, Xiaobai Li, Su-Jing Wang, Guoying Zhao, Yong-Jin Liu, Yu-Hsin Chen, and Xiaolan Fu. Casme ii: An improved spontaneous micro-expression database and the baseline evaluation. *PLoS one*, 9(1):e86041, 2014.
- [24] Adrian K Davison, Cliff Lansley, Nicholas Costen, Kevin Tan, and Moi Hoon Yap. Samm: A spontaneous micro-facial movement

- dataset. *IEEE Trans. Affective Comput.*, 9(1):116–129, 2016.
- [25] Petr Husák, Jan Cech, and Jiří Matas. Spotting facial micro-expressions “in the wild”. In *22nd Computer Vision Winter Workshop (Retz)*, pages 1–9, 2017.
- [26] Fangbing Qu, Su-Jing Wang, Wen-Jing Yan, He Li, Shuhang Wu, and Xiaolan Fu. *casme²*: a database for spontaneous macro-expression and micro-expression spotting and recognition. *IEEE Trans. Affective Comput.*, 9(4):424–436, 2017.
- [27] Xianye Ben, Yi Ren, Junping Zhang, Su-Jing Wang, Kidiyo Kpalma, Weixiao Meng, and Yong-Jin Liu. Video-based facial micro-expression analysis: A survey of datasets, features and algorithms. *IEEE Trans Pattern Anal Mach Intell.*, 44(9):5826–5846, 2021.
- [28] Xiaobai Li, Shiyang Cheng, Yante Li, Muzammil Behzad, Jie Shen, Stefanos Zafeiriou, Maja Pantic, and Guoying Zhao. 4dme: A spontaneous 4d micro-expression dataset with multimodalities. *IEEE Trans. Affective Comput.*, 14(4):3031–3047, 2022.
- [29] Senya Polikovsky, Yoshinari Kameda, and Yuichi Ohta. Facial micro-expressions recognition using high speed camera and 3d-gradient descriptor. *3rd International Conference on Imaging for Crime Detection and Prevention (ICDP 2009)*, 2009.
- [30] Matthew Shreve, Sridhar Godavarthy, Dmitry Goldgof, and Sudeep Sarkar. Macro-and micro-expression spotting in long videos using spatio-temporal strain. In *2011 IEEE international conference on automatic face & gesture recognition (FG)*, pages 51–56. IEEE, 2011.
- [31] Paul Ekman and Wallace V Friesen. Nonverbal behavior in psychotherapy research. In *Research in Psychotherapy Conference, 3rd, May-Jun, 1966, Chicago, IL, US*. American Psychological Association, 1968.
- [32] Diana Borza, Radu Danescu, Razvan Itu, and Adrian Sergiu Darabant. High-speed video system for micro-expression detection and recognition. *Sensors*, 17(12):2913, 2017.
- [33] Fan Zhang and Lin Chai. A review of research on micro-expression recognition algorithms based on deep learning. *Neural Comput. Appl.*, 36(29):17787–17828, 2024.
- [34] Xingcong Zhao, Ying Liu, Tong Chen, Shiyuan Wang, Jiejia Chen, Linwei Wang, and Guangyuan Liu. Differences in brain activations between micro-and macro-expressions based on electroencephalography. *Front. Neurosci.*, 16:903448, 2022.
- [35] Georgia Sandbach, Stefanos Zafeiriou, Maja Pantic, and Lijun Yin. Static and dynamic 3d facial expression recognition: A comprehensive survey. *Image Vision Comput.*, 30(10):683–697, 2012.
- [36] Paul Ekman and Wallace V Friesen. Facial action coding system. *Environmental Psychology & Nonverbal Behavior*, 1978.
- [37] Su-Jing Wang, Wen-Jing Yan, Guoying Zhao, Xiaolan Fu, and Chun-Guang Zhou. Micro-expression recognition using robust principal component analysis and local spatiotemporal directional features. In *Computer Vision-ECCV 2014 Workshops: Zurich, Switzerland, September 6-7 and 12, 2014, Proceedings, Part I 13*, pages 325–338. Springer, 2015.
- [38] Yong-Jin Liu, Jin-Kai Zhang, Wen-Jing Yan, Su-Jing Wang, Guoying Zhao, and Xiaolan Fu. A main directional mean optical flow feature for spontaneous micro-expression recognition. *IEEE Trans. Affective Comput.*, 7(4):299–310, 2015.
- [39] Liangfei Zhang, Ongjen Arandjelovic, and Xiaopeng Hong. Facial action unit detection with local key facial sub-region based multi-label classification for micro-expression analysis. In *Proceedings of the 1st Workshop on Facial Micro-Expression: Advanced Techniques for Facial Expressions Generation and Spotting*, pages 11–18, 2021.
- [40] Yandan Wang, John See, Raphael C-W Phan, and Yee-Hui Oh. Efficient spatio-temporal local binary patterns for spontaneous facial micro-expression recognition. *PLoS one*, 10(5):e0124674, 2015.
- [41] Hong-Xia Xie, Ling Lo, Hong-Han Shuai, and Wen-Huang Cheng. Au-assisted graph attention convolutional network for micro-expression recognition. In *Proceedings of the 28th ACM International Conference on Multimedia*, pages 2871–2880, 2020.
- [42] Zhe Sun, Zheng-ping Hu, Mengyao Zhao, and Shufang Li. Multi-scale active patches fusion based on spatiotemporal lbp-top for micro-expression recognition. *J. Visual Commun. Image Represent.*, 71:102862, 2020.
- [43] Sze-Teng Liong, Yee Siang Gan, John See, Huai-Qian Khor, and Yen-Chang Huang. Shallow triple stream three-dimensional cnn (ststnet) for micro-expression recognition. In *2019 14th IEEE international conference on automatic face & gesture recognition (FG 2019)*, pages 1–5. IEEE, 2019.
- [44] Zhaoliang Xia, Xiaopeng Hong, Xingyu Gao, Xiaoyi Feng, and Guoying Zhao. Spatiotemporal recurrent convolutional networks for recognizing spontaneous micro-expressions. *IEEE Transactions on Multimedia*, 22(3):626–640, 2019.
- [45] Yuchi Liu, Heming Du, Liang Zheng, and Tom Gedeon. A neural micro-expression recognizer. In *2019 14th IEEE international conference on automatic face & gesture recognition (FG 2019)*, pages 1–4. IEEE, 2019.
- [46] Ankith Jain Rakesh Kumar and Bir Bhanu. Micro-expression classification based on landmark relations with graph attention convolutional network. In *Proceedings of the IEEE/CVF conference on computer vision and pattern recognition*, pages 1511–1520, 2021.
- [47] Huai-Qian Khor, John See, Raphael Chung Wei Phan, and Weyiao Lin. Enriched long-term recurrent convolutional network for facial micro-expression recognition. In *2018 13th IEEE international conference on automatic face & gesture recognition (FG 2018)*, pages 667–674. IEEE, 2018.
- [48] Dae Hoe Kim, Wissam J Baddar, and Yong Man Ro. Micro-expression recognition with expression-state constrained spatiotemporal feature representations. In *Proceedings of the 24th ACM international conference on Multimedia*, pages 382–386, 2016.
- [49] Mohamed S Benlamine, Maher Chaouachi, Claude Frasson, and Aude Dufresne. Physiology-based recognition of facial micro-expressions using eeg and identification of the relevant sensors by emotion. In *International conference on physiological computing systems*, volume 2, pages 130–137. SciTePress, 2016.
- [50] Hodam Kim, Dan Zhang, Laehyun Kim, and Chang-Hwan Im. Classification of individual’s discrete emotions reflected in facial microexpressions using electroencephalogram and facial electromyogram. *Expert Syst. Appl.*, 188:116101, 2022.
- [51] Nastaran Saffaryazdi, Yenuska Goonesekera, Nafiseh Saffaryazdi, Nebiyou Daniel Hailemariam, Ebsa Girma Temesgen, Suranga Nanayakkara, Elizabeth Broadbent, and Mark Billingham. Emotion recognition in conversations using brain and physiological signals. In *Proceedings of the 27th International Conference on Intelligent User Interfaces*, pages 229–242, 2022.
- [52] Xingcong Zhao, Jiejia Chen, Tong Chen, Shiyuan Wang, Ying Liu, Xiaomei Zeng, and Guangyuan Liu. Responses of functional brain networks in micro-expressions: An eeg study. *Front. Psychol.*, 13:996905, 2022.
- [53] Xingcong Zhao, Jiejia Chen, Tong Chen, Ying Liu, Shiyuan Wang, Xiaomei Zeng, Jilong Yan, and Guangyuan Liu. Micro-expression recognition based on nodal efficiency in the eeg functional networks. *IEEE Trans. Neural Syst. Rehabil. Eng.*, 32:887–894, 2024.
- [54] Yiheng Han, Bingjun Li, Yu-Kun Lai, and Yong-Jin Liu. Cfd: A collaborative feature difference method for spontaneous micro-expression spotting. In *2018 25th IEEE International Conference on Image Processing (ICIP)*, pages 1942–1946. IEEE, 2018.
- [55] Vida Esmaeili and Seyed Omid Shahdi. Automatic micro-expression apex spotting using cubic-lbp. *Multimedia Tools and Applications*, 79:20221–20239, 2020.
- [56] Haoyuan Ma, Gaoyun An, Shengjie Wu, and Feng Yang. A region histogram of oriented optical flow (rhoof) feature for apex frame spotting in micro-expression. In *2017 International Symposium on Intelligent Signal Processing and Communication Systems (IS-PACS)*, pages 281–286. IEEE, 2017.
- [57] Hang Pan, Lun Xie, and Zhiliang Wang. Local bilinear convolutional neural network for spotting macro-and micro-expression intervals in long video sequences. In *2020 15th IEEE international conference on automatic face and gesture recognition (FG 2020)*, pages 749–753. IEEE, 2020.

- [58] Thuong-Khanh Tran, Quang-Nhat Vo, Xiaopeng Hong, Xiaobai Li, and Guoying Zhao. Micro-expression spotting: A new benchmark. *Neurocomputing*, 443:356–368, 2021.
- [59] Su-Jing Wang, Ying He, Jingting Li, and Xiaolan Fu. Mesnet: A convolutional neural network for spotting multi-scale micro-expression intervals in long videos. *IEEE Trans. Image Process.*, 30:3956–3969, 2021.
- [60] Zhihao Zhang, Tong Chen, Hongying Meng, Guangyuan Liu, and Xiaolan Fu. Smeconvnet: A convolutional neural network for spotting spontaneous facial micro-expression from long videos. *IEEE Access*, 6:71143–71151, 2018.
- [61] Michiel Verburg and Vlado Menkovski. Micro-expression detection in long videos using optical flow and recurrent neural networks. In *2019 14th IEEE International conference on automatic face & gesture recognition (FG 2019)*, pages 1–6. IEEE, 2019.
- [62] Giorgos Giannakakis, Dimitris Grigoriadis, Katerina Giannakaki, Olympia Simantiraki, Alexandros Roniotis, and Manolis Tsiknakis. Review on psychological stress detection using biosignals. *IEEE Trans. Affective Comput.*, 13(1):440–460, 2019.
- [63] Puneet Gupta, Brojeshwar Bhowmick, and Arpan Pal. Exploring the feasibility of face video based instantaneous heart-rate for micro-expression spotting. In *Proceedings of the IEEE Conference on Computer Vision and Pattern Recognition Workshops*, pages 1316–1323, 2018.
- [64] Ren Zhang, Ning He, Shengjie Liu, Ying Wu, Kang Yan, Yuzhe He, and Ke Lu. Your heart rate betrays you: multimodal learning with spatio-temporal fusion networks for micro-expression recognition. *International Journal of Multimedia Information Retrieval*, 11(4):553–566, 2022.
- [65] Anisa Putri Setyaningrum and Nugraha Priya Utama. Integrating attention and eulerian magnification for real time micro expression and heart rate detection. In *2024 International Conference on Artificial Intelligence, Blockchain, Cloud Computing, and Data Analytics (ICoABCD)*, pages 231–236. IEEE, 2024.
- [66] Haider Ismael Shahadi, Hayder J Albattat, Zaid Jabbar Al-allaq, and Ahmed Toman Thahab. Eulerian video magnification: a review. *Indones. J. Electr. Eng. Comput. Sci.*, 18(2):799, 2020.
- [67] Elias Rajaby and Sayed Masoud Sayedi. A structured review of sparse fast fourier transform algorithms. *Digital Signal Processing*, 123:103403, 2022.
- [68] Bochao Zou, Yingxue Wang, Xiaolong Zhang, Xiangwen Lyu, and Huimin Ma. Concordance between facial micro-expressions and physiological signals under emotion elicitation. *Pattern Recognition Letters*, 164:200–209, 2022.
- [69] Edoardo M Polo, Andrea Farabbi, Maximiliano Mollura, Alessia Paglialonga, Luca Mainardi, and Riccardo Barbieri. Comparative assessment of physiological responses to emotional elicitation by auditory and visual stimuli. *IEEE J. Transl. Eng. Health Med.*, 12:171–181, 2023.
- [70] Andrew T Jebb, Vincent Ng, and Louis Tay. A review of key likert scale development advances: 1995–2019. *Front. Psychol.*, 12:637547, 2021.
- [71] Mohsen Tavakol and Reg Dennick. Making sense of cronbach's alpha. *Int J Med Educ.*, 2:53, 2011.
- [72] Shradha Mehta, Rowena F Bastero-Caballero, Yijun Sun, Ray Zhu, Diane K Murphy, Bhushan Hardas, and Gary Koch. Performance of intraclass correlation coefficient (icc) as a reliability index under various distributions in scale reliability studies. *Stat Med.tavakol2011making*, 37(18):2734–2752, 2018.
- [73] Paul Ekman. Darwin, deception, and facial expression. *Annals of the new York Academy of sciences*, 1000(1):205–221, 2003.
- [74] Emad Barsoum, Cha Zhang, Cristian Canton Ferrer, and Zhengyou Zhang. Training deep networks for facial expression recognition with crowd-sourced label distribution. In *Proceedings of the 18th ACM international conference on multimodal interaction*, pages 279–283, 2016.
- [75] Xing Zhang, Lijun Yin, Jeffrey F Cohn, Shaun Canavan, Michael Reale, Andy Horowitz, Peng Liu, and Jeffrey M Girard. Bp4d-spontaneous: a high-resolution spontaneous 3d dynamic facial expression database. *Image Vision Comput.*, 32(10):692–706, 2014.
- [76] Patrick Lucey, Jeffrey F Cohn, Takeo Kanade, Jason Saragih, Zara Ambadar, and Iain Matthews. The extended cohn-kanade dataset (ck+): A complete dataset for action unit and emotion-specified expression. In *2010 IEEE computer society conference on computer vision and pattern recognition-workshops*, pages 94–101. IEEE, 2010.
- [77] Hakpyeong Kim and Taehoon Hong. Enhancing emotion recognition using multimodal fusion of physiological, environmental, personal data. *Expert Syst. Appl.*, 249:123723, 2024.
- [78] Jiehao Tang, Zhuang Ma, Kaiyu Gan, Jianhua Zhang, and Zhong Yin. Hierarchical multimodal-fusion of physiological signals for emotion recognition with scenario adaption and contrastive alignment. *Inf. Fusion*, 103:102129, 2024.
- [79] Xiao Han, Fuyang Chen, and Junrong Ban. Fmfnet: A fuzzy multimodal fusion network for emotion recognition in ensemble conducting. *IEEE Trans. Fuzzy Syst.*, 2024.
- [80] Jonghwa Kim. Bimodal emotion recognition using speech and physiological changes. *Robust speech recognition and understanding*, 265:280, 2007.
- [81] Hatice Gunes and Maja Pantic. Automatic, dimensional and continuous emotion recognition. *International Journal of Synthetic Emotions (IJSE)*, 1(1):68–99, 2010.
- [82] S Jerritta, M Murugappan, R Nagarajan, and Khairunizam Wan. Physiological signals based human emotion recognition: a review. In *2011 IEEE 7th international colloquium on signal processing and its applications*, pages 410–415. IEEE, 2011.
- [83] Guoying Zhao and Matti Pietikainen. Dynamic texture recognition using local binary patterns with an application to facial expressions. *IEEE Trans. Pattern Anal. Mach. Intell.*, 29(6):915–928, 2007.
- [84] Sze-Teng Liong, John See, KokSheik Wong, and Raphael C-W Phan. Less is more: Micro-expression recognition from video using apex frame. *Signal Process. Image Commun.*, 62:82–92, 2018.
- [85] Zhaoliang Xia, Wei Peng, Huai-Qian Khor, Xiaoyi Feng, and Guoying Zhao. Revealing the invisible with model and data shrinking for composite-database micro-expression recognition. *IEEE Trans. Image Process.*, 29:8590–8605, 2020.
- [86] Sirui Zhao, Hanqing Tao, Yangsong Zhang, Tong Xu, Kun Zhang, Zhongkai Hao, and Enhong Chen. A two-stage 3d cnn based learning method for spontaneous micro-expression recognition. *Neurocomputing*, 448:276–289, 2021.
- [87] Ling Zhou, Qirong Mao, Xiaohua Huang, Feifei Zhang, and Zhihong Zhang. Feature refinement: An expression-specific feature learning and fusion method for micro-expression recognition. *Pattern Recognition*, 122:108275, 2022.
- [88] Ruolin Li, Lu Wang, Tingting Yang, Lisheng Xu, Bingyang Ma, Yongchun Li, and Hongchao Wei. Micro-expression recognition by motion feature extraction based on pre-training. *arXiv preprint arXiv:2407.07345*, 2024.
- [89] Zhifeng Wang, Kaihao Zhang, Wenhan Luo, and Ramesh Sankaranarayanan. Htnet for micro-expression recognition. *Neurocomputing*, 602:128196, 2024.
- [90] Shuhuan Zhao, Shen Li, Yudong Zhang, and Shuaiqi Liu. Channel self-attention residual network: Learning micro-expression recognition features from augmented motion flow images. *IEEE Trans. Affective Comput.*, 2025.
- [91] Jinsheng Wei, Guanming Lu, Jingjie Yan, and Huaming Liu. Micro-expression recognition using local binary pattern from five intersecting planes. *Multimedia Tools Appl.*, 81(15):20643–20668, 2022.
- [92] Guanming Lu, Zhen Han, Jinsheng Wei, and Jingjie Yan. Learning discriminative features for micro-expression recognition. *Multimedia Tools Appl.*, 83(3):7761–7783, 2024.
- [93] John See, Moi Hoon Yap, Jingting Li, Xiaopeng Hong, and Su-Jing Wang. Megc 2019—the second facial micro-expressions grand challenge. In *2019 14th IEEE International Conference on Automatic*

- Face & Gesture Recognition (FG 2019)*, pages 1–5. IEEE, 2019.
- [94] R Meziati Sabour, Yannick Benezeth, F Marzani, K Nakamura, R Gomez, and F Yang. Emotional state classification using pulse rate variability. In *2019 IEEE 4th International Conference on Signal and Image Processing (ICSIP)*, pages 86–90. IEEE, 2019.
- [95] Richard D Lane, Kateri McRae, Eric M Reiman, Kewei Chen, Geoffrey L Ahern, and Julian F Thayer. Neural correlates of heart rate variability during emotion. *Neuroimage*, 44(1):213–222, 2009.
- [96] Foteini Agrafioti, Dimitris Hatzinakos, and Adam K Anderson. Ecg pattern analysis for emotion detection. *IEEE Trans. Affective Comput.*, 3(1):102–115, 2011.
- [97] Tam Pham, Zen Juen Lau, SH Annabel Chen, and Dominique Makowski. Heart rate variability in psychology: A review of hrv indices and an analysis tutorial. *Sensors*, 21(12):3998, 2021.
- [98] Madalena D Costa, Roger B Davis, and Ary L Goldberger. Heart rate fragmentation: a new approach to the analysis of cardiac interbeat interval dynamics. *Front Physiol.*, 8:255, 2017.
- [99] Junichiro Hayano, Masaya Kiso-hara, Norihiro Ueda, and Emi Yuda. Impact of heart rate fragmentation on the assessment of heart rate variability. *Appl. Sci.*, 10(9):3314, 2020.
- [100] Mariel Grassmann, Elke Vlemincx, Andreas Von Leupoldt, Justin M Mittelstädt, and Omer Van den Bergh. Respiratory changes in response to cognitive load: A systematic review. *Neural plasticity*, 2016(1):8146809, 2016.
- [101] Kyung Hwan Kim, Seok Won Bang, and Sang Ryong Kim. Emotion recognition system using short-term monitoring of physiological signals. *Med Biol Eng Comput.*, 42:419–427, 2004.
- [102] Wenqian Lin and Chao Li. Review of studies on emotion recognition and judgment based on physiological signals. *Applied Sciences*, 13(4):2573, 2023.
- [103] Dian Yu and Shouqian Sun. A systematic exploration of deep neural networks for eda-based emotion recognition. *Information*, 11(4):212, 2020.
- [104] Osmalina Nur Rahma, Alfian Pramudita Putra, Akif Rahmatillah, Yang Sa'ada Kamila Ariyansah Putri, Nuzula Dwi Fajriaty, Khusnul Ain, and Rifai Chai. Electrodermal activity for measuring cognitive and emotional stress level. *Journal of Medical Signals & Sensors*, 12(2):155–162, 2022.
- [105] Nastaran Saffaryazdi, Syed Talal Wasim, Kuldeep Dileep, Alireza Farrokhi Nia, Suranga Nanayakkara, Elizabeth Broadbent, and Mark Billingham. Using facial micro-expressions in combination with eeg and physiological signals for emotion recognition. *Front Psychol.*, 13:864047, 2022.
- [106] Vernon J Lawhern, Amelia J Solon, Nicholas R Waytowich, Stephen M Gordon, Chou P Hung, and Brent J Lance. Eegnet: a compact convolutional neural network for eeg-based brain-computer interfaces. *J. Neural Eng.*, 15(5):056013, 2018.
- [107] Wenhao Leng, Sirui Zhao, Yiming Zhang, Shiifeng Liu, Xinglong Mao, Hao Wang, Tong Xu, and Enhong Chen. Abpn: Apex and boundary perception network for micro-and macro-expression spotting. In *Proceedings of the 30th ACM International Conference on Multimedia*, pages 7160–7164, 2022.
- [108] Erheng He, Qianru Chen, and Qinghua Zhong. Sl-swin: a transformer-based deep learning approach for macro-and micro-expression spotting on small-size expression datasets. *Electronics*, 12(12):2656, 2023.
- [109] Jing Liu, Xin Li, Jiaqi Zhang, Guangtao Zhai, Yuting Su, Yuyi Zhang, and Bo Wang. Duration-aware and mode-aware micro-expression spotting for long video sequences. *Signal Process. Image Commun.*, 129:117192, 2024.
- [110] Henian Yang, Shucheng Huang, and Mingxing Li. Msf: A main and secondary bi-directional optical flow feature method for spotting micro-expression. *Neurocomputing*, 630:129676, 2025.
- [111] Shaoyuan Lu, Jingting Li, Yan Wang, Zizhao Dong, Su-Jing Wang, and Xiaolan Fu. A more objective quantification of micro-expression intensity through facial electromyography. In *Proceedings of the 2nd Workshop on Facial Micro-Expression: Advanced Techniques for Multi-Modal Facial Expression Analysis*, pages 11–17, 2022.